How Does Assimilating a Large Commercial GNSS RO Dataset Impact HAFS Hurricane Forecasts? An Evaluation in Support of the ROMEX Experiment

Submitted to Atmospheric Measurement Techniques

Revised in May 2026

Deleted: *Februar*

William J. Miller,[a] Yong Chen,[b] Shu-Peng Ho,[b] and Xi Shao[a]

Deleted:

[a]*Cooperative Institute for Satellite Earth System Studies (CISESS), Earth System Science Interdisciplinary Center, University of Maryland, College Park, MD, 20740, USA*

[b]*NOAA National Environmental Satellite, Data, and Information Service, Center for Satellite Applications and Research, College Park, MD, 20740, USA*

Corresponding author: Dr. William J. Miller, wmiller1@umd.edu

ABSTRACT

While Global Navigation Satellite System (GNSS) radio occultation (RO) data assimilation improves tropical cyclone (TC) intensity forecasts, the scaling of these impacts with RO observation volume remains unclear. This observing system experiment (OSE) study evaluates the impact of assimilating the large commercial GNSS RO profile dataset from the Radio Occultation Modeling EXperiment (ROMEX) on 84 Hurricane Analysis and Forecast System – configuration A (HAFS-A) model forecasts of four 2022 Atlantic hurricanes. The ROMEX dataset contains about 20,000 daily global Spire and PlanetiQ profiles, which is roughly triple the volume of government-provided RO data that the National Centers for Environmental Prediction (NCEP) assimilated operationally in 2022. Compared to a Control experiment that uses only operational RO data, assimilating ROMEX data together with operational RO profiles in HAFS-A yields ~ 5-15% relative skill improvement in minimum central sea-level pressure (P_{MIN}) absolute intensity forecast errors in short-range forecasts, and it nearly eliminates a ~ 2-3 hPa P_{MIN} over-intensification bias in medium-to-long range forecasts. Additionally, ROMEX commercial RO data assimilation reduces errors in HAFS-A temperature and water vapor in the middle-to-upper troposphere. A sensitivity experiment shows that lower-tropospheric RO data assimilated below the 5-km impact height contribute substantially to ROMEX forecast improvements relative to Control. These results demonstrate that quadrupling the volume of assimilated GNSS RO data yields a meaningful positive impact on regional model TC forecasts.

Formatted: Line spacing: 1.5 lines

Deleted: x

Deleted: errors

Deleted: provide a substantial

Deleted: contribution

1. Introduction

Global Navigation Satellite System (GNSS) radio occultation (RO) events occur when Low Earth Orbit (LEO) receiver satellites intercept radio signals transmitted by GNSS satellites [e.g., Global Positioning System (GPS), Global Navigation Satellite System (GLONASS)] that have passed through the Earth's atmosphere along limb soundings. Atmospheric refraction bends the RO ray, causing a delay in the received radio signal relative to its predicted phase in a vacuum. Processing centers, such as the University Corporation for Atmospheric Research (UCAR)'s COSMIC Data and Archive Center (CDAAC), use physics-based inversion techniques (Kuo et al., 2004) and precisely determined transmitter and receiver satellite positions to retrieve vertical profiles of the RO ray bending angle from Doppler-shifted occultation radio signals. RO bending angles can also be simulated from numerical weather prediction (NWP) model output using a forward operator that integrates atmospheric refractivity field gradients along an approximation of the RO ray path (Healy et al., 2007; Cucurull et al., 2013), since atmospheric refractivity depends on water vapor, temperature, and pressure.

GNSS RO bending angles have been assimilated in operational global NWP models over the last two decades, with their beneficial impacts on predicted temperature, wind, and pressure fields in the upper troposphere and lower stratosphere being well documented (Cucurull et al., 2013; Bonavita, 2014; Bowler, 2020; Lien et al., 2021). RO profiles complement satellite radiances in sampling atmospheric water vapor and temperature, offering high vertical resolution (sub 200 m), deep tropospheric signal penetration, and all-sky observability (Ho et al., 2020a; Schreiner et al., 2020). Additionally, RO bending angles serve as anchor data for radiance bias correction in NWP models (Poli et al., 2010) because they exhibit relatively unbiased errors above the boundary layer (Schreiner et al., 2020; Lien et al., 2021). Launched in June 2019, the joint US-Taiwan Formosa Satellite Mission-7/Constellation Observing System for Meteorology, Ionosphere, and Climate-2 (COSMIC-2) six-satellite constellation currently yields about 6,000 daily profiles globally, all within the ±45-degree° latitude band. Compared to previous missions, COSMIC-2 provides enhanced data coverage over the tropics (with approximately 5 daily profiles per 500 × × 500 km^2 box) and a higher signal-to-noise ratio (SNR), owing to improved receivers and digital beamforming antennas (Ho et al., 2020 b; Schreiner et al., 2020). Studies have demonstrated that tropospheric water vapor information derived from assimilating RO data

Formatted: Line spacing: 1.5 lines

Deleted:

Deleted: Since atmospheric refractivity depends on water vapor, temperature, and pressure,

Deleted: .

Deleted:

from COSMIC-2 or its predecessor mission could improve TC cyclogenesis detection in regional models (Liu, H. et al. 2012; Chen et al., 2020; Teng et al. 2021, 2023).

Despite a substantial increase in available GNSS RO data after the COSMIC-2 launch, the full benefits of assimilating these RO profiles into NWP models are likely not yet realized, due to their relatively sparse horizontal sampling density compared to satellite radiances. To theoretically evaluate how the forecast error improvement scales with RO profile volume, Harnisch et al. (2013) ran an ensemble of data-assimilation (EDA) experiments using the European Center for Medium-Range Weather Forecasts (ECMWF) global model. Using the reduction in ensemble spread as a proxy for forecast error reduction, they found incremental forecast improvement up to 128,000 globally assimilated profiles. Specifically, the improvement in upper-tropospheric temperature forecast error scaled logarithmically with the number of assimilated RO data, such that assimilating 16,000 daily profiles accounted for about 50% of the benefit from assimilating 128,000 daily profiles. Based on these findings, Harnisch et al. (2013) recommended 16,000 – 20,000 daily global RO profiles as the minimum number for optimal utilization in a global NWP system. Current government-owned GNSS RO receiver platforms, such as COSMIC-2 and the Meteorological Operational (Metop) satellites operated by the European Organization for the Exploitation of Meteorological Satellites (EUMETSAT), supply fewer than 10,000 daily global profiles to operational NWP centers.

Over the past five years, companies such as Spire Global and PlanetiQ have launched LEO satellites equipped with GNSS RO signal receivers. The US National Oceanic and Atmospheric Administration (NOAA), ECMWF, and other federal weather services worldwide are currently evaluating the benefits of assimilating commercial RO data into their operational NWP models. Data assimilation (DA) impact studies have found that augmenting government-provided RO data with relatively small commercial RO datasets is generally beneficial, at least to some degree. Lonitz et al. (2021) reported that assimilating about 5,000 daily Spire RO profiles, in addition to operationally assimilated RO data, into the global NWP models of both the UK Met Office and ECMWF reduced short-range temperature errors, with the most substantial improvement occurring in the extratropical upper troposphere when verified against radiosondes. Miller et al. (2025) evaluated the impacts of assimilating about 5,500 daily global Spire RO profiles in NOAA's Hurricane Weather Research and Forecasting (HWRF) model forecasts of four 2022 Atlantic hurricanes. They found that assimilating the Spire bending

Deleted:

Deleted: in NWP models are likely still not realized

Deleted: data

Deleted:

Deleted: re

Deleted: O

Deleted: Organisation

Deleted:

Deleted: profiles on top of operationally assimilated RO data in the global NWP models of both the UK Met Office and ECMWF reduced short-range temperature errors, with the most substantial improvement found angles along with operational government-provided RO data reduced HWRF's tropical cyclone (TC) minimum central sea-level pressure (P_{MIN}) over-intensification bias by 17-38% for medium-to-long range forecasts. However, this only improved P_{MIN} absolute errors for short-to-medium range lead times up to $t = 42$ h. They also showed that Spire assimilation reduced short-range water vapor errors measured against dropsondes in the lower troposphere, which was consistent with previous studies demonstrating that TC genesis and intensification can be sensitive to low-to-middle tropospheric water vapor fields in the storm environment at earlier times (Nolan 2007; Doyle et al. 2012; Teng et al. 2021). This sensitivity results partly from the fact that drier air from the TC environment can intrude into the core and suppress updraft development (Cram et al. 2007; Molinari et al. 2013). Updrafts help drive the conversion of latent heat extracted from the ocean to a TC's swirling wind kinetic energy (Rotunno and Emanuel, 1987).

The Radio Occultation Modeling EXperiment (ROMEX; Anthes et al., 2024) is a multi-center study evaluating the impacts of assimilating a large commercial GNSS RO dataset on retrospective operational NWP forecasts for the September-November 2022 period. More than 10 weather forecasting and research centers globally have participated, including NOAA, the Joint Center for Satellite Data Assimilation (JCSDA), ECMWF, the UK Met Office, Meteo-France, and the Korea Meteorological Administration. ROMEX seeks to demonstrate how DA scales with increasing numbers of RO observations and to validate the theoretical results of Harnisch et al. (2013) using real observations across a variety of operational NWP model configurations. ROMEX participants are assimilating the largest commercial RO dataset evaluated to date, comprising approximately 27,000 global daily commercial RO bending angle profiles, into their NWP systems.

This study supports ROMEX by evaluating the impact of assimilating a large commercial RO bending angle dataset, comprising about 20,000 Spire and PlanetiQ RO bending angle profiles per day globally[1], on Hurricane Analysis and Forecasting System – configuration A (HAFS-A) forecasts of four 2022 Atlantic hurricanes. Together with its "B" configuration, which uses different physics parameterizations and horizontal grid resolution, HAFS-A has provided NOAA with operational regional TC forecasting guidance since 2023. Our main objectives are to: (i) evaluate the extent to which assimilating an additional ~20,000 daily global commercial

[1] Our experiments do not use data from all ROMEX commercial providers.

Deleted: ,
Deleted: although
Deleted: data
Deleted: x
Deleted: ten
Deleted: data assimilation
Deleted: 0
Deleted: served as
Deleted: 's primary
Deleted: model
Deleted: benefit
Deleted: to HAFS regional TC intensity forecasts from
Formatted: Font: (Default) Times New Roman

RO profiles on top of operationally assimilated government-owned RO data benefits HAFS-A TC intensity forecasts; (ii) demonstrate how the assimilated ROMEX observation impacts vary across atmospheric layers and meteorological variables; and (iii) determine whether the ROMEX observations assimilated in the lower troposphere can positively impact HAFS-A forecasts, given the tendency for these observations to have larger retrieval or forward modeling errors leading to greater likelihood of rejection, compared to RO data from the middle or upper troposphere.

The remainder of this paper is organized as follows. Section 2 describes the selected hurricane cases, the HAFS-A model configuration, the ROMEX RO dataset, and the experimental design. Section 3 assesses how HAFS-A's DA system responds when provided with the ROMEX commercial RO profiles. Section 4 presents the impacts of assimilated RO data on forecast track, intensity, and gridded forecast field error statistics, and Section 5 describes a case study of these impacts on Hurricane Fiona (2022) forecasts. Section 6 provides a summary and concluding remarks.

2. Datasets and Methods

a) Selected TC cases

Figure 1 shows the observed tracks and Saffir-Simpson scale intensities of the four 2022 Atlantic hurricanes were selected for this study. These were the most significant TCs of the 2022 Atlantic season in terms of strength, longevity, and impacts, and computational constraints precluded running additional cases. Data are taken from the National Hurricane Center (NHC) Best Track archive (Jarvinen et al., 1984). Category 2 Hurricane Earl (2 – 10 September) and Category 4 Hurricane Fiona (14 – 23 September) were long-tracked storms that spent most of their time at hurricane intensity, defined as having maximum surface wind speed (V_{MAX}) exceeding 65 kt, outside the tropics (Blake 2023; Pasch et al. 2023). Both storms originated as African Easterly Wave (AEW) disturbances in the eastern tropical Atlantic, intensified as they encountered a moister environment around the Lesser Antilles, recurved northward around the western Atlantic ridge, and eventually underwent extratropical transition. Earl passed close enough to Bermuda to generate tropical-storm-force winds, and its outer rainbands caused heavy rainfall over Puerto Rico, leading to isolated flooding reports. Compared to Earl, Fiona was a more impactful storm. Fiona dropped 10-20 inches (254-508 mm) of rainfall over Guadeloupe and Puerto Rico, causing significant to catastrophic flash flooding on those islands. Fiona later made landfall as an extratropical storm on Nova Scotia with hurricane-force winds and a

Deleted: , with and without assimilation of COSMIC-2 data

Deleted: operator

Deleted: and/or

Deleted: there

Formatted: Indent: First line: 0"

minimum central pressure of 931 hPa, becoming the deepest cyclone on record to strike Canada. Fiona's flooding and winds caused seven direct fatalities in the Caribbean islands and Canada.

Major Hurricane Ian (23 – 30 September) also originated as an AEW and initially struggled to intensify while moving westward through the eastern and central Caribbean (Bucci et al. 2023). Late on 25 September, upper-level winds around the storm relaxed, enabling the vortex's upper- and lower-level centers to align vertically. Ian then underwent a 39-hour rapid intensification episode (Kaplan and DeMaria 2003) as it moved over an area of high ocean heat content, which ended with landfall in western Cuba. During this period Ian's V_{MAX} increased from 40 kt to 110 kt. After slightly weakening from the land interaction, Ian resumed intensifying in the southeastern Gulf of Mexico, and the storm made landfall at 1905 UTC on 28 September near Cape Coral, Florida, as a 130-kt Category 4 hurricane with a 4.6-meter peak storm surge. Ian caused 156 fatalities and an estimated $113 billion of damage in the US, making it the third most costly US hurricane on record. Category 1 Hurricane Julia (6 – 10 October 2022) developed and intensified in the southwestern Caribbean and struck Nicaragua (Cangialosi 2023). Moving across Central America, Julia caused severe flooding, leading to 35 fatalities. Please refer to the NHC tropical cyclone reports [Blake 2023 (Earl), Pasch et al. 2023 (Fiona), Bucci et al. 2023 (Ian), and Cangialosi 2023 (Julia)] for further details on the meteorology, damage impacts, and operational forecast assessments of these storms.

Deleted: 15

Deleted: foot

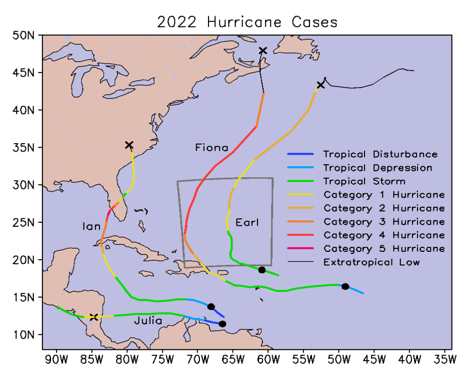

Figure 1. The observed tracks of the four 2022 Atlantic hurricanes selected for the ROMEX HAFS-A forecast experiments, with colors indicating the stage of TC development at the time. V_{MAX} stratifies hurricane intensity according to the Saffir-Simpson Scale: Category 1 (64-82 kt), Category 2 (83-95 kt), Category 3 (96-112 kt), Category 4 (113-136 kt), and Category 5 (above 136 kt). Closed circles and X-symbols mark the beginning and end, respectively, of each

Deleted:

Deleted: 7

hurricane's HAFS-A experiment cycling period. The dark gray polygon shows the HAFS-A moving nest boundaries for the 0600 UTC 07 September Hurricane Earl analysis.

b) HAFS-A model configuration and RO data assimilation algorithm

This study uses version 2.0 of NOAA's HAFS-A, a regional forecasting model operationally activated by the National Centers for Environmental Prediction (NCEP) to forecast a single TC following its cyclogenesis in the Atlantic or eastern Pacific basins. HAFS-A v2.0 is dual nested with two-way feedback between a fixed ~ 75° × 75° sized outer domain with 5.4-km horizontal resolution and a TC-following ~ 12° × 12° sized nest with 1.8-km horizontal resolution. The 81-level sigma pressure hybrid vertical coordinate system has a 2-hPa model top, and its lower boundary is coupled to the Modular Ocean Model version 6 (MOM6). Initial conditions and lateral boundary conditions for the outer domain are provided by NOAA's operational Global Forecasting System (GFS). The Gridpoint Statistical Interpolation (GSI; Wang et al. 2013) software assimilates observations into HAFS-A's moving nest every six hours using a Four-dimensional Ensemble Variational (4DEnVar) algorithm that extracts flow-dependent background error covariances from the 80-member operational GFS ensemble. Assimilated observations include temperature, humidity, and winds from conventional platforms (radiosondes, ships, and buoys); GNSS RO bending angles; microwave and infrared satellite radiances; and in-situ data from aircraft reconnaissance missions (dropsondes, High Density Observations from aircraft sensors, and Tail Doppler Radar-measured winds).

Deleted: HAFS configuration A (

Deleted:)

Deleted: TC

Deleted: following

Deleted: features

Deleted: ,

Deleted: coupled to the Modular Ocean Model version 6 (MOM6).…

Assimilating observations into a background vortex that poorly estimates a TC's intensity, structure, or position can cause analysis degradations because a TC's inner core can feature sharp horizontal gradients of wind, temperature, and water vapor (Christophersen et al. 2022). To mitigate this potential problem, HAFS-A adjusts 6-h forecast fields within the moving nest using a vortex initialization (VI) algorithm during each DA cycle, prior to assimilating observations (Liu et al. 2020). The VI procedure relocates the background vortex's kinematic and thermodynamic fields to the position estimated by the real-time Tropical Cyclone Vitals Database (TCVitals; Trahan and Sparling 2012). It then adjusts these fields to better match the TCVitals V_{MAX}, P_{MIN}, and storm size while keeping relative humidity (RH) unchanged. The background vortex is normally extracted from the 6-h HAFS-A forecast initialized from the previous cycle, unless the storm is very weak (TCVitals $V_{MAX} < 20$ m s^{-1}), in which case the 6-h operational GFS-forecast vortex is used. In either case, HAFS-A pastes the background vortex

Deleted: mprovement

Deleted: TCVitals data (

onto the operational GFS's 6-h forecast environmental fields interpolated to the moving nest. Therefore, the HAFS-A DA system does not cycle background fields between the TC vortex edge and the moving nest boundaries, although these fields are modified by observations assimilated in the current cycle.

HAFS-A assimilates RO bending angles occurring within a $\pm$ 3-hour window around the analysis time using the NCEP Bending Angle Model (NBAM; Cucurull et al. 2013; Cucurull and Purser 2023), a one-dimensional forward operator. NBAM estimates RO bending angle observation errors using a piecewise exponential function of the observation's impact height with default tunable coefficients that have been determined from GFS background and analysis departure statistics using the Desrosiers et al. (2005) method. The HAFS-GSI quality control (QC) algorithm rejects RO observations that could adversely affect the analysis. Most rejections are triggered either by a "statistical check" when the fractional observation-minus-background (O-B) innovation | O–B |/O exceeds a latitude, height, and temperature-dependent cutoff value, or by the RO ray's tangent point being located within or below a background super-refractivity (SR) layer where the vertical refractivity gradient exceeds 75 percent of the -157 N-units km^{-1} critical threshold. The SR rejections are necessary because NBAM can yield an indeterminate solution for observations located inside or below a SR layer (Cucurull, 2015; Cucurull and Purser 2023).

c) ROMEX RO observation dataset

The ROMEX dataset used in this study contains approximately 26,000 daily global RO bending-angle profiles. EUMETSAT processed all ROMEX profiles, except for the COSMIC-2 data, which UCAR provided. The largest data volume comes from Spire, which provides about 16750 profiles per day globally, followed by the COSMIC-2, PlanetiQ, and *Metop-B/C* missions, which contribute about 4900, 2750, and 1150 profiles per day, respectively (Anthes et al., 2024). Prior to a December 2024 code upgrade, GSI implementations with NCEP's forecasting models rejected all Metop bending angles below the 8-km impact height (~ 650 hPa) based on prior work finding larger Metop-A/B departures against the GFS background (Dutta et al., 2019). Since our HAFS-GSI build predates the removal of this QC check, the assimilated Metop-B/C profiles are expected to have little impact on the forecast lower- to middle-tropospheric temperature and water vapor fields. The government-owned *TerraSAR-X, TanDEM-X, and KOMPSAT-5* missions together contribute up to 500 daily global profiles. The ROMEX

Deleted: forecast
Deleted: are not cycled
Deleted: is larg
Deleted: e.
Deleted: bout
Deleted: bending
Deleted: with the
Deleted: except
Deleted: ion
Deleted: of
Deleted: were
Deleted: by UCAR
Deleted: *O*
Deleted: daily
Deleted: to-middle

commercial bending angles are assigned the same observation errors and QC settings as those used for COSMIC-2, except that their QC cutoff threshold rejects all data above the 30-km impact height, whereas COSMIC-2 and other government missions use 50 km. This follows the default settings for commercial RO data in the operational HAFS-GSI.

d) RO Data Impact Experiment Design

To demonstrate the impacts of assimilating the ROMEX commercial observations, COSMIC-2, and all lower-tropospheric RO data, four independent HAFS-A observing system experiments (OSEs) are run as follows:

(i) Control, assimilating only data from government-owned missions (primarily COSMIC-2 and *Metop*);

(ii) Control_noC2, the same as Control except without assimilating COSMIC-2;

(iii) ROMEX, assimilating the full ROMEX dataset; and

(iv) ROMEX_noLowlevRO, like ROMEX except that all RO data below the 5-km impact height are rejected.

The 5-km height threshold is chosen for ROMEX_noLowlevRO because it serves as a reasonable proxy for the top of the moist lower troposphere where many processes important to TC intensification occur (Montgomery & Smith, 2014), and because HAFS-GSI checks RO bending angles below this height for background SR conditions (Section 2b). Among these experiments, Control most closely replicates the RO dataset assimilated in NOAA's 2022 operational NWP models[2], which included approximately 5500 daily Spire profiles through the Commercial Weather Data Pilot (CWDP) program during that year's Atlantic hurricane season. The operational GFS provides the initial and boundary conditions for HAFS-A's outer domain during each DA cycle in all four experiments. Therefore, since HAFS-A only assimilates observations in the moving nest, this study measures the impacts of assimilated GNSS RO observations on a TC vortex and its near-storm environment within a few hundred kilometers. Each experiment begins with a HAFS-A cold start initialized soon after TC cyclogenesis (Fig. 1). The HAFS-A analysis is then cycled over a multi-day period, with each analysis initializing a 120-h HAFS-A free forecast (run without further observation assimilation). The last HAFS-A

[2] In 2022 NOAA was operationally using the Hurricane Weather Research and Forecasting (HWRF) model for regional TC forecasting guidance. HAFS-A and HAFS-B became operational the following year.

Deleted: RO observation
Deleted: heigh
Deleted: is set to
Deleted: 45
Deleted:
Deleted: compared to 505 km for
Deleted: *Denial*
Deleted: F
Deleted: data denial
Deleted: *O*
Deleted: and
Deleted: impact

analysis is initialized soon after final landfall for Fiona, Ian, and Julia, and shortly before Earl's extratropical transition.

3. GNSS RO Data Assimilation Statistics

a. RO data retention and quality control in HAFS-GSI

Figure 2a shows the number of Spire, PlanetiQ, and COSMIC-2 profiles available for assimilation in HAFS-A during each Hurricane Fiona analysis cycle. As expected, Spire provides the largest volume of RO data, although the number of profiles overlapping the ~12° × 12° domain varies substantially across different analysis cycles, ranging from one to thirty-one. Anthes et al. (2024) observed a bimodal distribution in the local time sampling density of ROMEX Spire profiles, with peaks at 0900-1200 and 2100-0000 (see their Fig. 12), which they attributed to the Spire satellites' sun-synchronous polar orbits. Spire's bimodal local time sampling pattern is not easily discernible during periods when the HAFS-A nest has limited zonal movement, such as 20-22 September, when Fiona remains over the US Eastern Daylight Time zone's (GMT - 4 h) longitudinal range while moving mostly northward east of the Bahamas (Fig. 1). This is not surprising, given the HAFS-A nest's relatively small size and wide (6-h) DA window. Therefore, we attribute the differences in Spire profile availability over DA cycles mostly to variability in Spire occultation swath locations over the TC case study periods. Table 1 lists the number of RO profiles assimilated per day in the Control_noC2, Control, and ROMEX experiments for each TC case. Over the full evaluation period, the addition of Spire and PlanetiQ data in ROMEX increases the assimilated profile count 4.4-fold for Earl, 3.8-fold for Fiona, 3.3-fold for Ian, and 1.8-fold for Julia, relative to Control. Earl and Fionas' larger gain in RO data volume from Control to ROMEX is consistent with those storms spending more time outside the tropics (Fig. 1), where COSMIC-2 data have sparser coverage (Ho et al. 2020b). A total of 129, 717, and 2513 RO profiles are assimilated in the Control_noC2, Control, and ROMEX experiments respectively.

Formatted: Line spacing: single

Deleted: Ian

Deleted: The figure also shows the number of profiles with at least one bending angle that passes GSI's QC checks below 700 hPa. …

Deleted: data assimilation

Deleted: fewer than 5

Deleted: over

Deleted: 20

Deleted: Hurricane Ian's

Deleted: 7

Deleted: - 01 October period

Deleted: the storm

Deleted: variability

Deleted: randomness

Deleted: We also find more comparable Spire and COSMIC-2 profile counts when the nest is at its lowest latitudes, namely for Ian during its 23-26 September tropical depression and tropical storm phases. This is consistent with the COSMIC-2 sampling density peaking close to the Equator, where it is comparable to the ROMEX Spire profile density (Anthes et al. 2024).

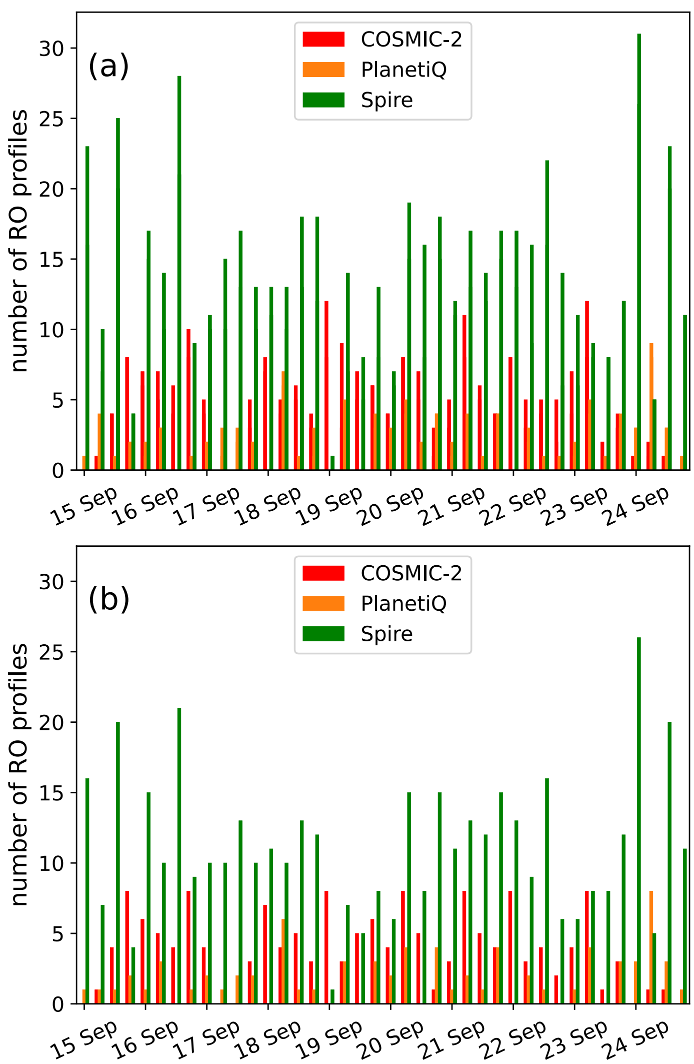

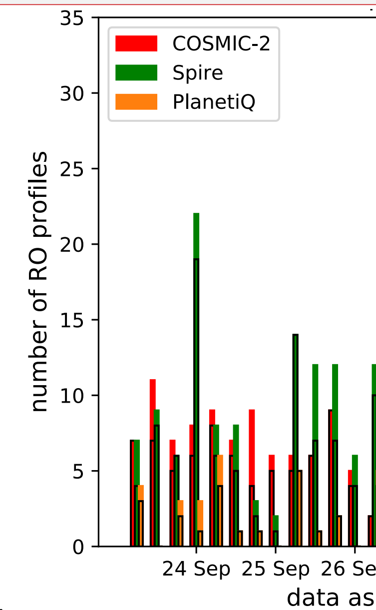

Figure 2. (a) Number of COSMIC-2, PlanetiQ, and Spire GNSS RO profiles available for assimilation in the HAFS-A moving nest for individual Hurricane Fiona (2022) DA cycles, shown as red, orange, and green bars, respectively. Each 0000 UTC cycle time is labeled with its date on the *x*-axis. (b) As in (a), except showing the number of profiles with at least one bending angle assimilated below 800 hPa.

Deleted: Spire, and

Deleted: each

Deleted: Ian

Deleted: data assimilation

Deleted: green, and

Deleted: Embedded black-outlined open bars

Deleted: 7

Date (N_{cyc})	Earl noC2	Earl Control	Earl ROMEX	Fiona noC2	Fiona Control	Fiona ROMEX	Ian noC2	Ian Control	Ian ROMEX	Julia noC2	Julia Control	Julia ROMEX
03 Sep (3)	1	19	73	—	—	—	—	—	—	—	—	—
04 Sep (4)	2	24	92	—	—	—	—	—	—	—	—	—
05 Sep (4)	4	22	83	—	—	—	—	—	—	—	—	—
06 Sep (4)	4	22	86	—	—	—	—	—	—	—	—	—
07 Sep (4)	4	17	69	—	—	—	—	—	—	—	—	—
08 Sep (4)	3	17	101	—	—	—	—	—	—	—	—	—
09 Sep (4)	3	27	97	—	—	—	—	—	—	—	—	—
10 Sep (4)	4	13	101	—	—	—	—	—	—	—	—	—
15 Sep (4)	—	—	—	4	17	87	—	—	—	—	—	—
16 Sep (4)	—	—	—	6	30	104	—	—	—	—	—	—
17 Sep (4)	—	—	—	4	14	80	—	—	—	—	—	—
18 Sep (4)	—	—	—	1	24	97	—	—	—	—	—	—
19 Sep (4)	—	—	—	6	40	85	—	—	—	—	—	—
20 Sep (4)	—	—	—	5	27	101	—	—	—	—	—	—
21 Sep (4)	—	—	—	3	29	100	—	—	—	—	—	—
22 Sep (4)	—	—	—	5	28	102	—	—	—	—	—	—
23 Sep (4,3)	—	—	—	5	30	82	4	29	58	—	—	—
24 Sep (4,4)	—	—	—	6	10	96	9	42	94	—	—	—
25 Sep (4)	—	—	—	—	—	—	4	31	79	—	—	—
26 Sep (4)	—	—	—	—	—	—	4	19	58	—	—	—
27 Sep (4)	—	—	—	—	—	—	6	18	84	—	—	—
28 Sep (4)	—	—	—	—	—	—	5	25	105	—	—	—
29 Sep (4)	—	—	—	—	—	—	4	21	103	—	—	—
30 Sep (4)	—	—	—	—	—	—	5	25	84	—	—	—
01 Oct (2)	—	—	—	—	—	—	5	12	61	—	—	—
06 Oct (2)	—	—	—	—	—	—	—	—	—	3	15	33
07 Oct (4)	—	—	—	—	—	—	—	—	—	6	38	56
08 Oct (4)	—	—	—	—	—	—	—	—	—	3	24	40
09 Oct (2)	—	—	—	—	—	—	—	—	—	1	8	22
Total	25	161	702	45	249	934	46	222	726	13	85	151

Table 1. Number of GNSS RO profiles assimilated for the Control_noC2 (noC2), Control (CTRL), and ROMEX experiments in the 12° × 12° HAFS-A moving nest for each day that overlaps a TC case cycling period. Dashes indicate that no HAFS DA cycles occurred for that storm on that day, as identified by the column and row respectively. Numbers in parentheses list the number of DA cycles for a given day, with the maximum value of four indicating that observations were assimilated in the 00, 06, 12, and 18 UTC cycles. The comma-delimited values for 23 and 24 September indicate that the HAFS-A nest assimilated profiles for both the Fiona and Ian cases, with the Fiona cycling period ending at 18 UTC 24 Sep and the Ian cycling period beginning at 06 UTC 23 Sep. The sets of profiles assimilated for Fiona and Ian on 23-24 Sep were different and non-overlapping due to differences in the HAFS-A nest location for the two storms.

Figure 2b highlights a key challenge: for some COSMIC-2 and commercial RO profiles, all bending angles below 800 hPa are rejected by HAFS-GSI's QC checks and not assimilated. This is critical because TC intensification is highly sensitive to water vapor distribution in the lower-to-middle troposphere around the storm (e.g., Nolan 2007; Doyle et al. 2012; Teng et al. 2021). The GSI QC algorithm is known to reject the largest percentage of RO data in the lower-

Deleted: also
Deleted: a substantial fraction of
Deleted: available
Deleted: lack assimilated data
Deleted: 7

to-middle troposphere (Miller et al. 2023, 2025; Lien et al. 2021), primarily due to greater bending angle retrieval uncertainty caused by water vapor effects (Kursinski et al. 1997; Kuo et al. 2004; Anthes et al. 2022). Further work is needed to determine whether HAFS-GSI's QC criteria are optimally set for all RO data platforms.

Figure 3 presents histograms of COSMIC-2, Spire, and PlanetiQ bending angle rejection percentages binned by pressure level for all checks (Fig. 3a) and the statistical O-B outlier check (Fig. 3b). The bins extend up to 15 hPa, which is below the 30-km high altitude cutoff used for commercial RO data. All three platforms show similar retention statistics above 950 hPa that are mostly caused by the statistical O-B check (cf. 3a, 3b), with the total rejection rate increasing from ~20% in the 700-450 hPa layer to ~55% in the 950-850 hPa layer (Fig. 3a). Notably, below 950 hPa, Spire's O-B rejection percentage is almost 10% smaller than that of COSMIC-2. Since GSI uses the same empirically-determined |O-B|/O rejection thresholds for COSMIC-2 and commercial RO data, this indicates that Spire has a lower frequency of extreme O-B outliers within and near the boundary layer than COSMIC-2. Almost all other tropospheric RO observation rejections are triggered by the super-refractivity check, which mainly depends on the background refractivity field (Cucurull 2015).

Deleted: s

Deleted: a and 3b

Deleted:

Deleted: s

Deleted: tropospheric

Deleted: . The majority of GSI's bending angle rejections between 950 and 50 hPa result from their |O-B|/O exceeding an empirically determined threshold (Section 2b) for COSMIC-2, Spire (cf. 3a, 3c), and PlanetiQ (cf. 3b, 3d).

Deleted: (rectangular boxed region in Fig. 3c)

Deleted: both platforms

Deleted: This is an interesting result, considering that Spire RO data generally have a lower signal-to-noise ratio than COSMIC-2 (Ho et al. 2023).

Deleted: In the stratosphere above 25 hPa, the commercial data show a higher rejection rate than COSMIC-2, due to the former having a lower QC cutoff height.

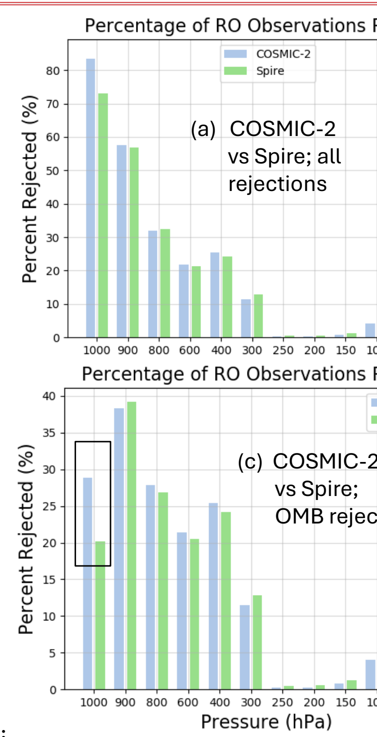

Deleted:

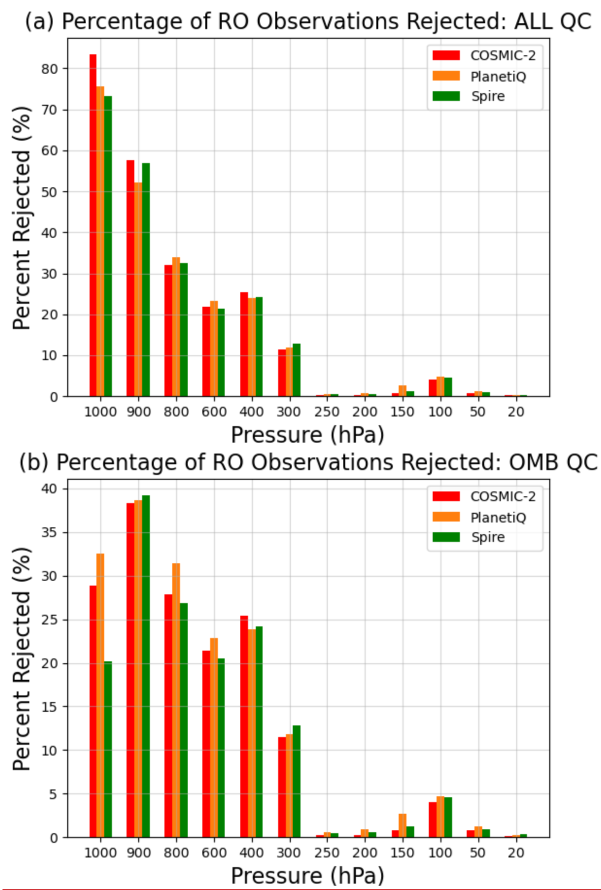

Figure 3. (a) Percentage of RO bending angle observations binned by pressure level that are rejected by HAFS-GSI QC screens. Pressure level height (hPa) bins labeled on the abscissa as 1000, 900, 800, 600, 400, 300, 250, 200, 150, 100, 50, and 20 are bounded as > 950, 950-850, 850-700, 700-450, 450-350, 350-275, 275-225, 225-175, 175-125, 125-75, 75-25 and 25-15 hPa, respectively. Red, orange, and green bars show COSMIC-2, PlanetiQ, and Spire rejection percentages respectively. (b) As in (a), except showing only the percentage of observations rejected by the statistical check for O-B outliers.

b. Diagnosed RO observation uncertainty

Figure 4 compares profiles of COSMIC-2, Spire, and PlanetiQ observation error standard deviations estimated from the ROMEX experiment's O-B and observation-minus-analysis (O-A) data collected from all four TC cases. These diagnosed observation errors include contributions

Formatted: Indent: Left: 0"

Deleted: Top row [

Deleted: and (b)]:

Deleted: p

Deleted: <

Deleted: 2

Deleted: rejection percentages (blue bars) are compared to Spire rejection percentages (green bars) in (a) and

Deleted: (orange bars) in (b)

Deleted: Bottom row [(c) and (d)]:

Deleted: a

Deleted: and (b)

Deleted: observation-minus-background (OMB)

Deleted: check

Formatted: Font: Italic

Formatted: List Paragraph, Outline numbered + Level: 2 + Numbering Style: a, b, c, … + Start at: 1 + Alignment: Left + Aligned at: 0.75" + Indent at: 1"

Deleted: statistics using the Desroziers et al. (2005) method.

Deleted: This algorithm,

Deleted: widely used by operational NWP centers (Cucurull et al. 2013; Bonavita 2014; Bowler 2020; Lien et al. 2021), uses a forecast model's diagnostic output dataset

Deleted: to estimate the diagonal elements of the RO bending angle observation error matrix, which

Deleted: s

from instrument, retrieval, and representative sources, and we estimated them using the Desroziers et al. (2005) algorithm, which has been widely employed by operational NWP centers (Cucurull et al. 2013; Bonavita 2014; Bowler 2020; Lien et al. 2021). Some caution is warranted in drawing broader conclusions about the uncertainty characteristics of these three RO observation platforms, given our relatively small DA diagnostic data sample drawn from a TC-following regional domain. From our experiments, we find that all three platforms have similar observation uncertainty in the upper troposphere. However, Spire observations show the smallest uncertainty below the 5-km impact height in the tropics (Fig. 4a) and below the 7-km impact height in the extratropics (Fig. 4b).

Deleted: .

Deleted: W

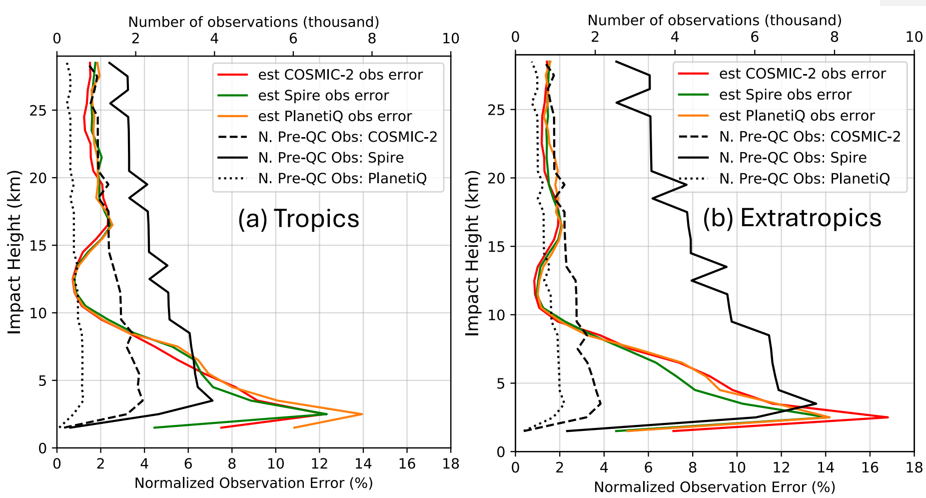

Figure 4. RO bending angle observation error standard deviation profiles estimated by the Desroziers et al. (2005) method for (a) the tropics and (b) the extratropics. The red, green, and orange lines show COSMIC-2, Spire, and PlanetiQ errors, respectively. Dashed, solid, and dotted black lines, respectively, show the number of COSMIC-2, Spire, and PlanetiQ observations per height bin that were used in the error estimation.

4. HAFS-A Forecast Verification Statistics

Deleted: Objective verification using the full

Deleted: f

Deleted: set

a. TC track and intensity forecasts

We now evaluate the impacts of assimilating ROMEX and COSMIC-2 RO observations on HAFS-A TC track and intensity forecasts verified against the NHC's Best Track dataset. Forecasts initialized during the first 48 cycling hours (containing eight analysis cycles) are not used for computing verification statistics to allow HAFS-A time to "spin up" and respond to the accumulative impacts of assimilated observations. Figure 5a compares the mean absolute TC position errors across the four experiments as a function of forecast lead time. Also shown is the number of Control forecasts used for averaging, which decreases with increasing lead time because the HAFS-A TC vortex tracker does not provide output for storms that have weakened after landfall or moved near the edge of the fixed outer domain. Differences in TC position error among the four experiments are generally small, which is not surprising given that TC motion is often most sensitive to larger-scale flows driven by synoptic weather features far from the storm (Chan and Gray 1982; Galarneau and Davis 2013). The HAFS-A model's 12° × 12° storm-following nest receives the same GFS-provided initial and lateral boundary conditions from its surrounding outer domain in all four experiments (Section 2b).

Nevertheless, we find that assimilating the commercial RO observations has a small positive impact on TC position errors during the t = 18-102 h period, as evidenced by the positive ROMEX relative skill versus Control (Fig. 5b). When analyzing mean absolute error (err) statistics from a set of forecasts, we define relative skill for each sensitivity experiment (EXP) as $(err_{Control} - err_{EXP})/err_{Control}$. Control_noC2's negative relative skill during the same period (Fig. 5b) indicates that COSMIC-2 observations are also beneficial for TC track forecasts. This is particularly true for the subset of analyses that initialize TCs equatorward of 24° N, for which removing COSMIC-2 from Control yields negative 5-10% relative skill during t = 54-96 h (not shown). We hypothesize that these small- to medium-range track forecast improvements, gained from assimilating COSMIC-2 and commercial RO data in the HAFS-A moving nest, could come from improved model predictions of TC vortex size, depth, or circulations in the near-storm environment, which in turn influence the storm's response to larger-scale flow fields (Galarneau and Davis 2013).

Deleted: 78

Deleted: its absolute error difference from Control, normalized by the Control absolute error.

Formatted: Font: Italic

Deleted: HAFS

Deleted: HAFS

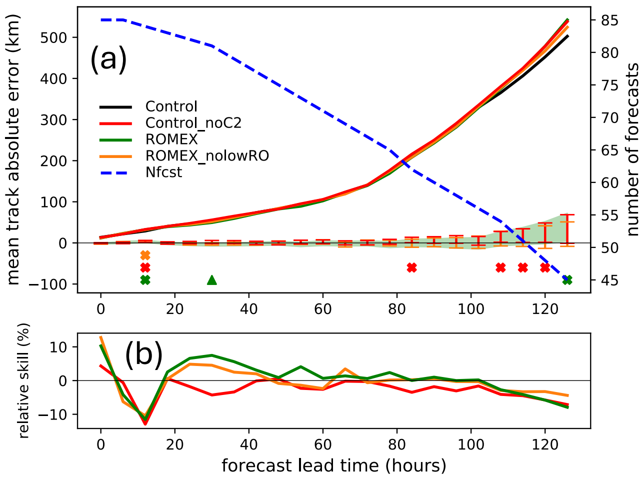

Figure 5. (a) Mean absolute errors in TC position (km) plotted as a function of forecast lead time for the Control (black line), Control_noC2 (red line), ROMEX (green line), and ROMEX_nolowRO (orange line) HAFS-A experiments. Errors are measured against the NHC Best Track data. The dashed blue line shows the number of available verification forecasts. Green shading shows the 90% confidence interval of the ROMEX-minus-Control forecast TC position error difference generated by bootstrap resampling. Statistically significant larger (smaller) ROMEX errors relative to Control occur at times when these confidence intervals remain above (below) zero, as denoted by green cross symbols (triangles). Red (orange) error bars and colored symbols likewise show ROMEX_noC2-minus-Control (ROMEX_noLowlevRO-minus-Control) forecast TC position error confidence intervals and statistically significant differences. (b) Time series of the TC position forecast relative skill (%) for the Control_noC2 (red line), ROMEX (green line), and

Deleted: HAFS

ROMEX_noLowlevRO (orange line) experiments.

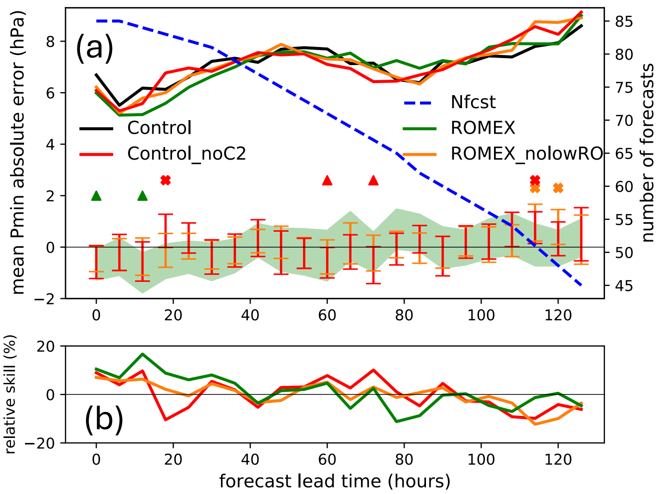

Figure 6. As in Fig. 5, but for TC P_{MIN} intensity (hPa).

Figure 6 compares time series of P_{MIN} mean absolute error for the HAFS-A experiments. ROMEX commercial observations are modestly beneficial through t = 36 h, when they provide a ~ 5-15% relative skill improvement, which is statistically significant for 0-h and 12-h forecasts. A substantial portion of ROMEX's t = 0-36 h relative skill improvement is lost when RO data below the 5-km impact height are removed (compare green and orange curves in Fig. 6b). COSMIC-2 impacts on forecast P_{MIN} intensity mean absolute errors are mixed. Assimilating the ROMEX commercial observations nearly eliminates Control's negative 2-3 hPa mean P_{MIN} bias over the t =24-90 h period (Figure 7). COSMIC-2 assimilation partially contributes to Control's P_{MIN} over-intensification bias, as shown by comparing the red and black curves in Figure 7.

Deleted: HAFS

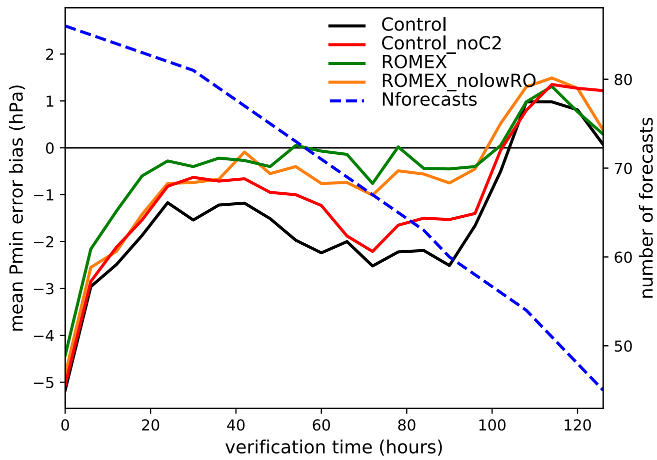

Figure 7. Forecast time series of TC P_{MIN} mean bias (hPa) for the Control (black line), Control_noC2 (red line), ROMEX (green line), and ROMEX_noLowlevRO (orange line) experiments, along with the number of forecasts used for verification (dashed blue line).

c. *Verification against ERA5 data*

Formatted: Line spacing: 1.5 lines

We next compare the HAFS-A experiments in terms of their forecast temperature and water vapor errors, using the ECMWF Reanalysis version 5 (ERA5) as the verification truth. Figure 8a shows that assimilating ROMEX commercial RO data reduces the temperature Root-Mean-Square Deviation (RMSD) in the 200-400 hPa layer by several percentage points relative to Control over most of the forecast period. This improvement in ROMEX temperature RMSD extends down to around 800 hPa between t = 18 h and t = 48 h. In the lower troposphere, the impacts of ROMEX commercial RO observation impacts on temperature RMSD are mixed, showing degradation over the first 18 hours but mostly improvement after t = 54 h. Regarding bias, Figure 8b shows that Control has a cool bias in the lower troposphere and a warm bias in the mid-to-upper troposphere. Assimilating the ROMEX commercial RO observations has little impact on the HAFS-A temperature bias patterns, except for a slight mitigation of the warm bias between 200 and 400 hPa in the later forecast period. Compared to the ROMEX commercial RO data, the assimilated COSMIC-2 observations have more mixed and muted impacts on the HAFS-A temperature fields, as evidenced by the Control and Control_noC2 temperature RMSD and bias field comparisons shown in Figures 8c and 8d, respectively.

Differences between the Control-normalized temperature RMSDs shown in Figures 8a and 8e reflect the impacts of RO data assimilated below 5 km. Removing all lower-tropospheric RO observations from the ROMEX configuration (Fig. 8e) results in a substantial portion of the ROMEX temperature RMSD improvement (relative to Control) below 600 hPa (Fig. 8a) being lost. Predictably, the temperature RMSD improvement in the upper troposphere is largely retained in ROMEX_noLowlevRO. This outcome is expected, as localization in the HAFS-A background-error covariance matrix should cause assimilated observation impacts to dampen with increasing vertical distance from the observation.

Overall, assimilating ROMEX commercial RO data reduces random errors in HAFS-A forecast tropospheric water vapor. Similar to temperature, the ROMEX specific humidity RMSD is reduced by several percentage points relative to Control over most layers and times in the middle and upper troposphere, with mixed impacts in the lower troposphere (Fig. 9a). Some of the most substantial improvement occurs during analyses and short-range forecasts around 500 hPa, where the ROMEX specific humidity RMSD is 3-6% smaller than Control. The ROMEX commercial RO data have a modest drying impact; they mitigate a Control moist bias in the 400-700 hPa layer but exacerbate a Control dry bias in short-to-medium range forecasts below 850 hPa (Fig. 9b). However, these ROMEX-minus-Control specific humidity mean error differences are quite small, generally less than 0.1 g kg^{-1}.

Deleted: forecast

Unlike the mixed results for temperature, COSMIC-2 observations show a clearer positive impact on water vapor fields, as evidenced by the widespread specific humidity RMSD degradation in Control_noC2 relative to Control (Fig. 9c). COSMIC-2 assimilation also yields mixed and generally very small changes in HAFS-A water vapor mean biases (Fig. 9d). Finally, removing all (commercial- and government-mission) RO data below 5 km in ROMEX_noLowlevRO causes nearly all water vapor RMSD improvement below 400 hPa in ROMEX to be lost (cf. 9a, 9e). This implies that lower-tropospheric RO observations can also improve HAFS-A water vapor estimates in the middle troposphere via the background-error covariance matrix.

Deleted: (

Deleted:)

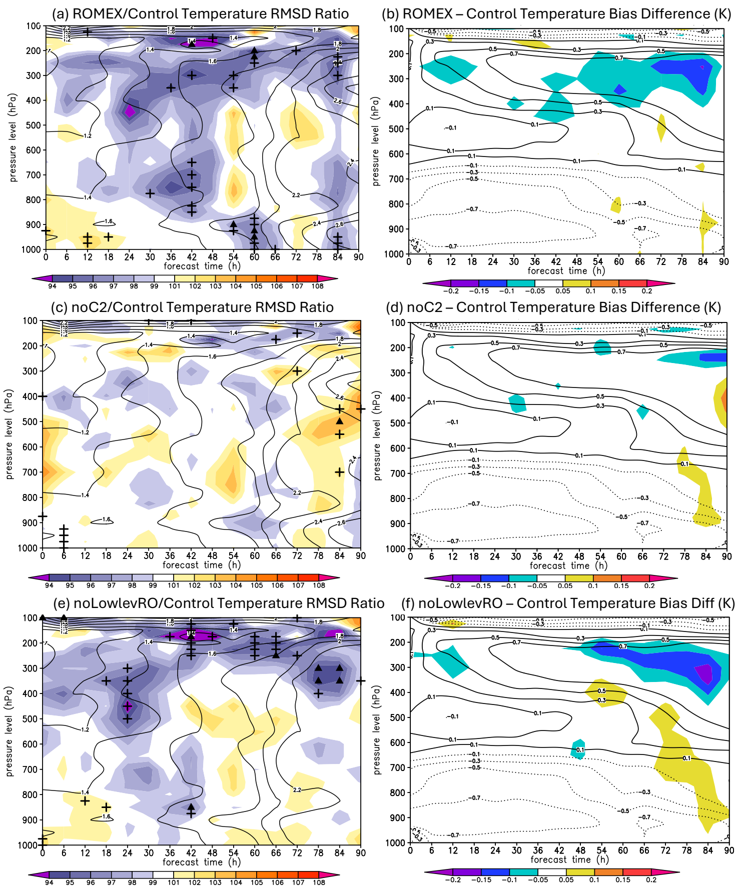

Figure 8. (a) Time-height plot showing the ratio of the ROMEX forecast temperature RMSD divided by the Control forecast temperature RMSD (shading, %), where the RMSD is computed with respect to the ERA5 within 300 km of the TC center. Black contours show the Control temperature RMSD (K). Crosses and triangles show times and layers where the difference between the Control and ROMEX temperature RMSD is statistically significant at the 95% and 99% level, respectively. (b) Time-height plot showing the difference between the ROMEX and Control temperature biases [(ROMEX – ERA5) – (Control – ERA5)] in shading (K), with the Control temperature bias (K) also plotted in black contours. (c) As in (a), but for the Control_noC2/Control temperature RMSD ratio. (d) As in (b), but for the Control_noC2-Control temperature bias difference. (e) As in (a), but for the ROMEX_noLowlevRO/Control temperature RMSD ratio. (f) As in (b), but for the ROMEX_noLowlevRO-Control temperature bias difference.

Deleted: X-minus

Deleted: -

Deleted:)

Deleted: with respect to the ERA5

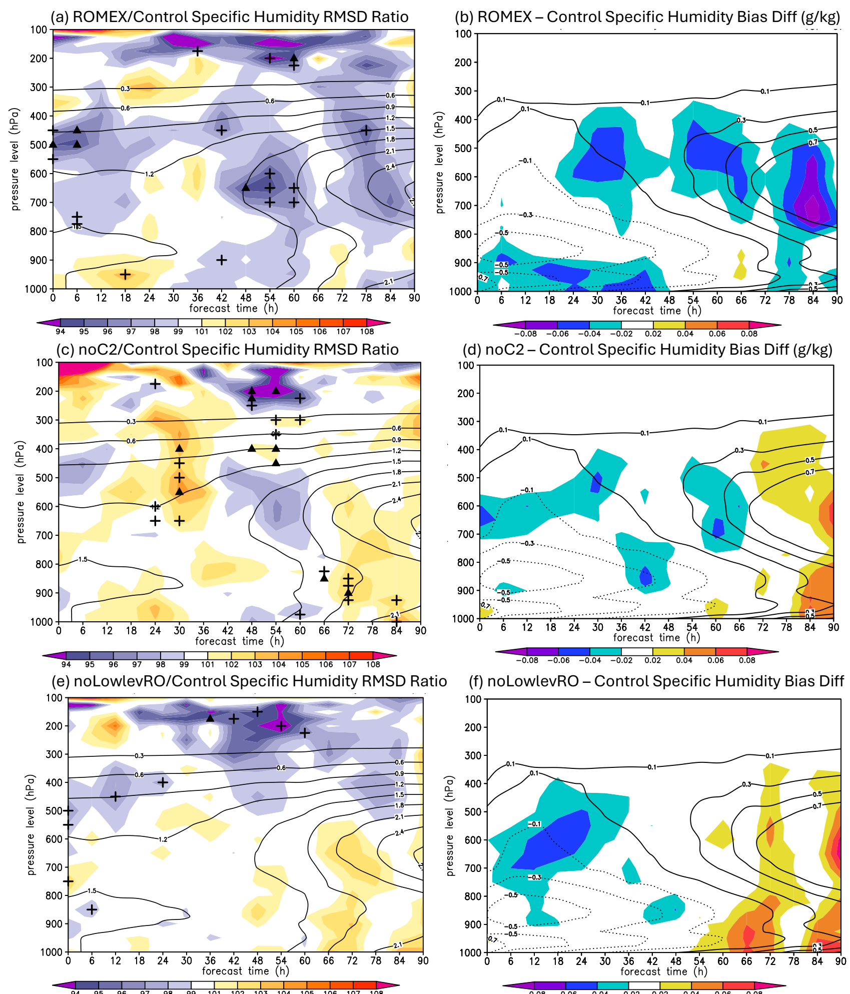

Figure 9. As in Figure 8, but for the HAFS-A specific humidity RMSD (g kg^{-1}).

Deleted: ¶ ... [1]

d. Verification against dropsonde observations

NOAA P-3 reconnaissance aircraft sampled Hurricanes Earl, Fiona, and Ian at 12-24-hour intervals during their intensification and mature phases. Flying around 10,000 ft, the P-3 aircraft crossed the TC inner core in several transect legs while releasing GPS dropsondes and collecting other in-situ observations. Two NOAA Gulfstream-IV missions also flew into

Fiona's near-storm environment and released upper-tropospheric dropsondes. For verification, we compute 12-h HAFS-A forecast errors for temperature, specific humidity, and wind speed from 21 initialization cycles (7 from Earl, 7 from Fiona, 6 from Ian, and 1 from Julia; see Table 2) against dropsondes available within ±3 hours of the verification time. Dropsondes were equipped with GPS sensors, enabling tracking of their three-dimensional trajectories during free fall. Since most dropsondes were collected by the lower-flying P-3 missions, our verification is restricted to the sub-700 hPa layer.

Deleted: 1

Case	Initialization time (UTC)	Aircraft platform	Number of dropsondes
Earl	1200 05 September	NOAA P-3	14
Earl	0000 06 September	NOAA P-3	18
Earl	1200 06 September	NOAA P-3	17
Earl	0000 07 September	NOAA P-3	26
Earl	1200 07 September	NOAA P-3	16
Earl	0000 08 September	NOAA P-3	26
Earl	1200 08 September	NOAA P-3	22
Fiona	0000 17 September	NOAA P-3	19
Fiona	0000 18 September	NOAA P-3	23
Fiona	1200 18 September	NOAA G-IV	5
Fiona	1200 19 September	NOAA P-3	21
Fiona	0000 20 September	NOAA P-3	25
Fiona	1200 20 September	NOAA P-3 and G-IV	42
Fiona	1200 21 September	NOAA P-3	17
Ian	1200 25 September	NOAA P-3	1
Ian	0000 26 September	NOAA P-3	27
Ian	1200 26 September	NOAA P-3	18
Ian	0000 27 September	NOAA P-3	13
Ian	1200 27 September	NOAA P-3	4
Ian	0000 28 September	NOAA P-3	11
Julia	1200 08 October	NOAA P-3	25

Table 2. List of all HAFS-A 12-h forecasts verified against aircraft reconnaissance mission dropsonde data.

Deleted: 1

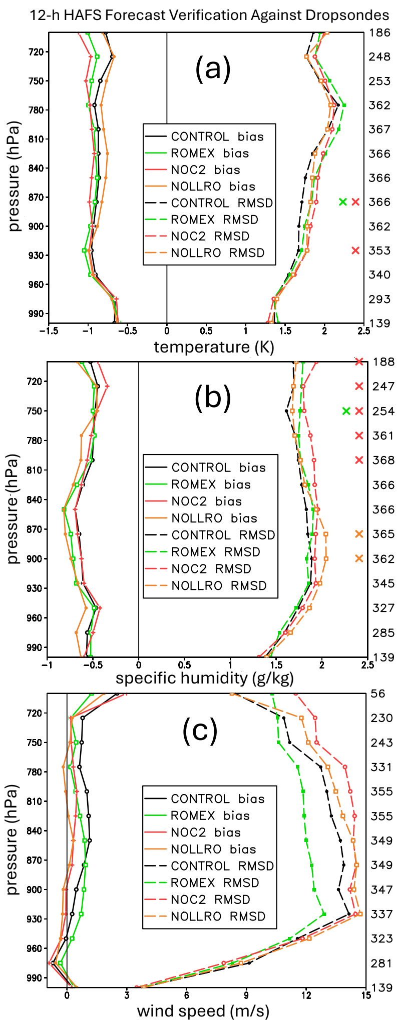

Figure 10. (a) Solid lines show profiles of the 12-h HAFS-A temperature forecast bias (K) computed against NOAA aircraft reconnaissance mission dropsondes for Control (black), ROMEX (green), Control_noC2 (red), and ROMEX_noLowlevRO (orange). The number of dropsonde temperature observations per verification layer is shown on the right *y*-axis. Dashed lines show the 12-h HAFS-A forecast temperature RMSD (K) relative to dropsonde data, colored by experiment. (b) As in (a) but for 12-h forecast specific humidity (g kg^{-1}). (c) As in (a) but for 12-h forecast horizontal wind speed (m s^{-1}). Green, red, and orange X-symbols, respectively, mark layers where the ROMEX, Control_noC2, and ROMEX_noLowlevRO forecast RMSDs differ statistically significantly from the Control RMSD at the 95% level.

Deleted: HAFS

Deleted: HAFS

Figure 10a compares the 12-h forecast temperature biases and RMSDs of the four HAFS-A experiments against collocated dropsonde temperature observations. Control shows a negative 0.5–1 K cool bias in the sub-700 hPa layer. Compared to Control, the ROMEX temperature bias profile is similar, with one exception: it shows a ~0.25 K stronger cool bias in the 700-750 hPa layer. Removing the sub-5 km RO data from our ROMEX experiment reduces the cool-temperature bias in this layer, bringing it closer to that of Control, suggesting that sub-5 km RO observations drive the ROMEX experiment's degradation there. The Control_noC2 cool bias is also ~ 0.25 K stronger than Control's between 700 and 750 hPa, indicating a positive impact from assimilating COSMIC-2 in that layer. For temperature RMSD, both the ROMEX and ROMEX_noLowlevRO are comparable to or larger than Control's over the sub-700 hPa layer. However, assimilating COSMIC-2 in Control yields a 0.1-0.2 K RMSD improvement over Control_noC2 within a large portion of the sub-700 hPa layer.

For the 12-h forecast specific humidity verification (Fig. 10b), we find that Control has a ~ 0.5 g kg^{-1} dry bias below 700 hPa, and that ROMEX's dry bias is similar or slightly worse. RO data assimilated below 5 km are slightly beneficial, as removing them increases the dry bias by ~ 0.1 g kg^{-1} over portions of the sub-700 hPa layer. COSMIC-2 assimilation has little impact on Control's dry bias. While the ROMEX specific humidity RMSD profile resembles that of Control, the RO data assimilated below 5 km are generally beneficial for reducing random water vapor errors, particularly around 900 hPa. At this level, the ROMEX_noLowlevRO specific humidity RMSD is a statistically significant ~ 0.2 g kg^{-1} larger than those of both ROMEX and Control. Above 800 hPa, COSMIC-2 assimilation in Control also yields a statistically significant ~ 0.2 g kg^{-1} specific humidity RMSD improvement over Control_noC2.

The assimilated ROMEX RO data improves the horizontal wind speed RMSD by ~ 1-2 m s^{-1} in the 750-950 hPa layer, although this result is not statistically significant. Removing all sub-5 km RO data more than reverses all of ROMEX's wind RMSD improvement, and additionally, removing the COSMIC-2 observations degrades the Control wind RMSD. Therefore, the lower-tropospheric RO dataset from Spire, PlanetiQ, and COSMIC-2 is beneficial for reducing random horizontal wind-speed errors below 750 hPa in HAFS-A. Even though the RO forward operator does not depend on kinematic variables, this result is consistent with Chen et al. (2020), who showed that cycled RO refractivity assimilation in a regional model could improve short-range

Deleted: the

forecasts of vertical velocity and vorticity during TC cyclogenesis via dynamical coupling between thermodynamic and kinematic fields.

5. ROMEX Observation Impacts on the Structure and Intensity of Hurricane Fiona (2022)

After examining individual HAFS-A forecasts from all four cases, it was found that Hurricane Fiona intensity forecasts initialized on 21 and 22 September stood out from the rest for their greater improvement when assimilating the ROMEX data. This is shown in Fig. 11, which compares the Control and ROMEX P_{MIN} forecast time series against Best Track P_{MIN} for the eight 21-22 September initialization cycles. During this period, Fiona's intensification rate slowed as the Category 4 storm reached a steady state while moving northeastward through the subtropical North Atlantic about 1000 km off the southeastern US coast. Favorable environmental conditions, including warm sea surface temperatures (SSTs) and low vertical wind shear (VWS), maintained Fiona's mature TC structure and 930-935 hPa P_{MIN} through 12 UTC 23 September. Except for the 06 UTC 21 September cycle (Fig. 11a), the Control P_{MIN} forecasts shown here feature a persistent 10-20 hPa over-intensification (i.e., negative) bias starting at the model initialization. Assimilating the ROMEX dataset yields a ~ 5-10 hPa mitigation of Control's negative P_{MIN} analysis and forecast bias. The track forecasts initialized on 21 and 22 September show minimal differences between the Control and ROMEX experiments (not shown).

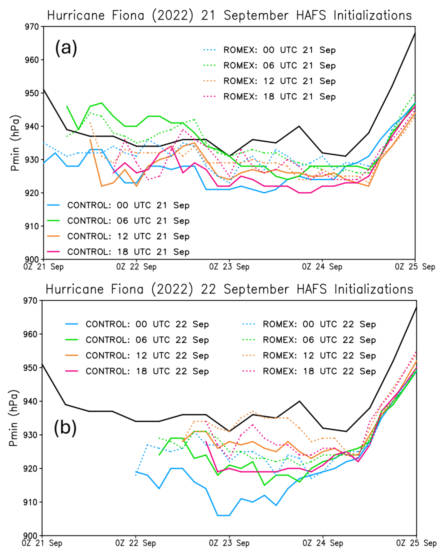

Figure 11. Hurricane Fiona (2022) P_{MIN} forecasts initialized on (a) 21 September and (b) 22 September, shown for Control (solid lines) and ROMEX (dotted lines). Lines plotting forecast P_{MIN} time series are colored by initialization time, as indicated in the inset key boxes. The black line shows the NHC Best Track P_{MIN} for Fiona.

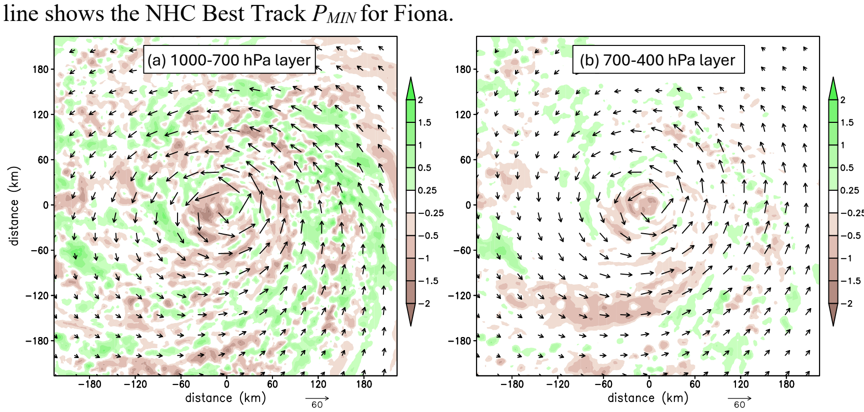

Figure 12. (a) ROMEX-minus-Control specific humidity differences (g kg^{-1}) averaged over the 1000-700 layer and over the 00, 06, 12, and 18 UTC 21 September analyses. Vectors show ROMEX 900-hPa horizontal winds (m s^{-1}) averaged over the same four analyses. (b) As in (a) but for ROMEX-minus-Control specific humidity differences averaged over the 700-400 hPa layer with 500-hPa ROMEX horizontal winds.

This persistent pattern of reduced over-intensification biases in ROMEX initializations on 21-22 September suggests that the ROMEX DA cycles led to the evolution of a less favorable near-storm environment. Figure 12a shows ROMEX-minus-Control analysis specific humidity differences averaged vertically below 700 hPa and temporally over the 00, 06, 12, and 18 UTC cycles on 21 September. Most areas inside the 100-km radius are 0.25-1 g kg^{-1} drier in ROMEX, compared to Control. This is consistent with our finding of drier 12-h ROMEX forecasts versus Control along inner-core P-3 dropsonde trajectories in the 825-925 hPa layer (Fig. 10b). Beyond the 100-km radius, particularly in the storm's northeastern quadrant, the ROMEX lower troposphere analysis is found to be moister than that of Control. Examining ROMEX-minus-Control specific humidity analysis differences averaged in the 700-400 hPa mid-troposphere layer for the same four cycles (Fig. 12b), the most prominent differences are evident near the TC center as well as in a band about 120 km to the south and southwest, where ROMEX analyses are about 0.25-1 g kg^{-1} drier.

Figure 13 compares Hurricane Fiona's structure in 12-h Control and ROMEX forecasts initialized at 12 UTC 21 September. While both the Control- (Fig. 13a) and ROMEX-forecast (Fig. 13b) storms' convective patterns share many characteristics, including a prominent rainband located in the northeastern quadrant around 2 degrees' radius from the center, the Control storm has higher reflectivity values within its eyewall. The latter appears here as the annular-shaped region around Fiona's center where 900-hPa horizontal wind speeds exceed 50 m s^{-1}. Compared to ROMEX, the Control forecast's near-surface eyewall winds are about 5-10 m s^{-1} stronger, broadly consistent with these forecasts' P_{MIN} differences (compare the dotted and solid orange lines at 00 UTC 22 September in Fig. 11a) under an empirical TC vortex pressure-wind relationship (Chavas et al., 2025). Control also generates stronger and more organized midlevel updrafts, arcing around the ~ 0.3-degree radius in the northern and southeastern quadrants of its eyewall (cf. 13c, 13d). These differences in reflectivity and mid-level updraft strength between the Control and ROMEX 12-h forecasts reveal that the Control has more vigorous inner-core convection, which aligns with its analysis showing a moister lower-to-middle troposphere within a 100-km radius (Fig. 12). This is dynamically significant: deep convective updrafts in a TC inner core provide a key mechanistic link between the favorable thermodynamic conditions of high relative humidity (RH) in the lower-to-middle troposphere and the storm's wind field intensification. For example, it is well known that eyewall updrafts facilitate latent heat conversion to kinetic energy (Rotunno & Emanuel, 1987) and convergence of higher absolute angular momentum (AAM) air advected inward from larger radii (Zhang et al., 2001;

Deleted: dynamical

Moved (insertion) [1]

Deleted: and

Deleted: .These deep updrafts enhance

Deleted: the

Deleted: air from outer regions into the inner core, increasing the eyewall tangential wind speed in the middle troposphere due to AAM conservation and in the boundary layer when AAM advection overcomes frictional dissipation (Montgomery and Smith 2014). Additionally, eyewall updrafts facilitate vortex deepening through vertical advection of AAM

Deleted: 2

Montgomery and Smith, 2014). A moister near-storm environment limits dry air entrainment and favors stronger, more organized eyewall updrafts (Cram et al., 2007; Braun et al. 2012). Therefore, it is plausible that the drying impact of the assimilated ROMEX observations on Hurricane Fiona's 21 September analyses helped to reduce the storm's over-intensification bias in HAFS-A forecasts initialized from those analyses.

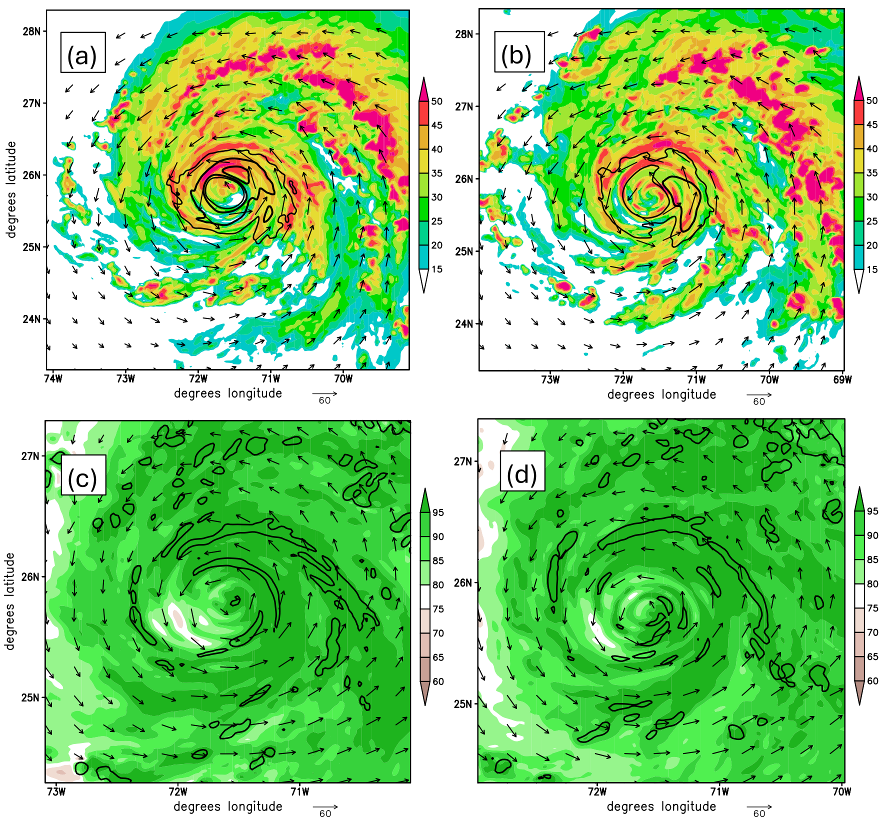

Figure 13. (a) Control 12-h forecast of Hurricane Fiona (2022) composite radar reflectivity (shading, dBZ) valid at 00 UTC 22 Sep. Horizontal winds at 900 hPa (m s^{-1}) are shown as vectors (see arrow scale at lower right) and their magnitudes are contoured (thin for 50 and thick for 55 and 60). (b) As in (a) but for the ROMEX experiment. (c) Same Control 12-h forecast shown in (a), but here plotting 700-400 hPa layer-averaged RH (shading, %), the 1-m s^{-1} vertical velocity contour at 600 hPa, and 500-hPa horizontal wind vectors (m s^{-1}). (d) As in (c) but for the ROMEX experiment.

Deleted:

Moved up [1]: These deep updrafts enhance the convergence of higher absolute angular momentum (AAM) air from outer regions into the inner core, increasing the eyewall tangential wind speed in the middle troposphere due to AAM conservation and in the boundary layer when AAM advection overcomes frictional dissipation (Montgomery and Smith 2014). Additionally, eyewall updrafts facilitate vortex deepening through vertical advection of AAM (Zhang et al. 2002) and

Deleted: and the tilting of horizontal relative vorticity filaments into the vertical direction (Chen et al. 2018).

Deleted: likely

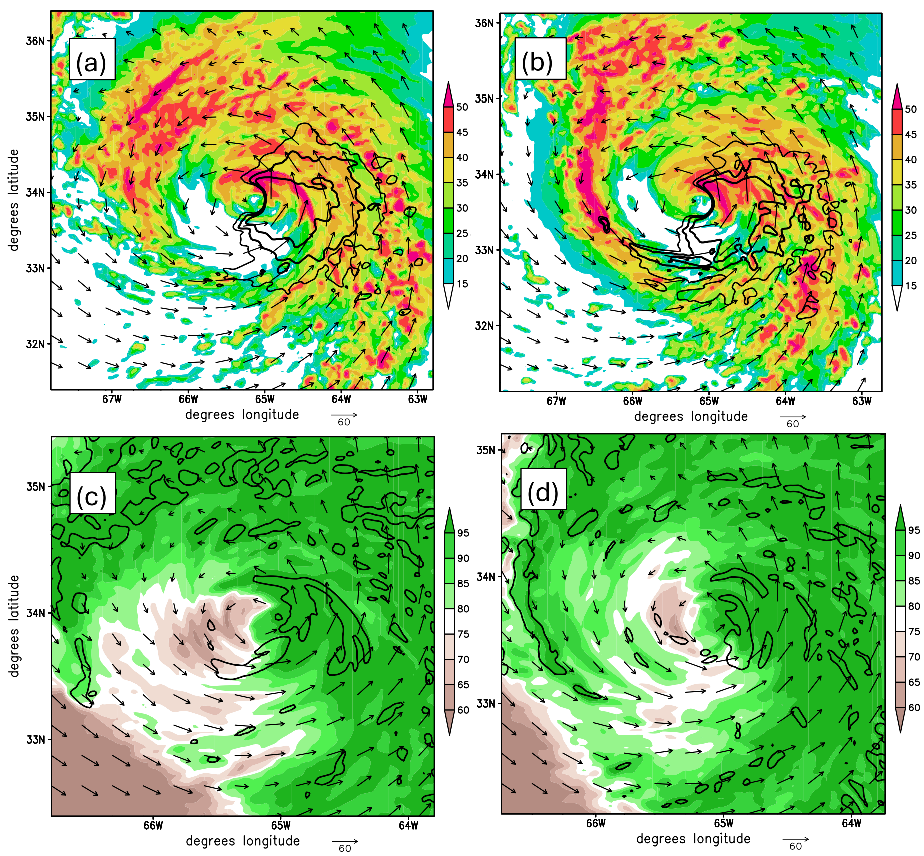

Figure 14. As in Fig. 13, but for 48-h forecasts valid at 12 UTC 23 Sep.

Revisiting these Control and ROMEX forecasts thirty-six hours later at 12 UTC 23 September, we find more similar intensities, both in terms of their 900-hPa wind speed, which exceeds 60 m s^{-1} in the eastern quadrant (Figs. 14a and 14b), and in their ~ 930 hPa P_{MIN} (orange lines in Fig. 11a). Compared to the 12-h forecast, Fiona's inner-core reflectivity, horizontal wind (Figs. 14a, 14b), and updraft (Figs. 14c, 14d) structures are more asymmetric. Meanwhile, southwesterly 850-200 hPa VWS ahead of an upper-level trough moving off the northeastern US coast has strengthened from 11.0 m s^{-1} to 12.9 m s^{-1} over the past 36 hours, according to the NHC's Statistical Hurricane Intensity Prediction Scheme (SHIPS; DeMaria et al. 2005) analysis. Differential advection of TC eyewall vorticity with height caused by moderate-to-strong VWS

Deleted: This asymmetry is influence
Deleted: d
Deleted: by
Deleted: increasing
Deleted: , which
Deleted: s
Deleted: 21.4 kt
Deleted: 5
Deleted: 0
Deleted: kt
Deleted: 00 UTC 22 - 12 UTC 23 September period

creates a more favorable (unfavorable) environment for deep convection on the vortex's downshear (upshear) side (DeMaria 1996; Jones 1995; Chen et al. 2018), which could account for the asymmetries shown in Fig. 14. Broadly consistent with the Best Track, both the Control and ROMEX forecasts initialized at 12 UTC 21 Sep maintain Fiona's intensity in a quasi-steady state for the next 24 hours, after which the storm weakens (Fig. 11a) while undergoing extratropical transition (Pasch et al., 2023). Although beyond the scope of this study, we speculate that Fiona's weakening resulted from a combination of cooling SSTs and the disruptive impacts of moderate-to-strong VWS on the vortex structure (Simpson and Riehl, 1958; Frank and Ritchie, 2001). Predominating influences from these larger-scale environmental conditions, which are not affected by DA in the HAFS-A nest (Section 2b), would be consistent with the relatively small differences between the Control and ROMEX intensity forecasts during this later period of Fiona's lifecycle (Fig. 11).

6. Summary and Conclusions

This study evaluated the impacts of assimilating the ROMEX GNSS RO bending angle dataset on 84 HAFS-A regional model forecasts of four 2022 Atlantic hurricanes. The ROMEX dataset contains about 20,000 daily global commercial RO profiles from Spire and PlanetiQ, processed by EUMETSAT, as well as government-owned RO data. Spire provided the bulk of the ROMEX observations – about 16750 per day globally, and their observation error standard deviation diagnosed from HAFS-A O-B and O-A statistics was found to be smaller than that of COSMIC-2 in most layers of the lower-to-middle troposphere. HAFS-A assimilated RO observations that passed QC checks within its ~ 12° × 12° TC-following domain.

Compared to a Control experiment using only the government-owned RO dataset containing about 7,000 daily global profiles, ROMEX assimilation yielded a modest ~ 5-15% relative skill improvement in P_{MIN} absolute intensity forecast errors through t = 36 h, with mixed results at longer lead times. Additionally, ROMEX assimilation nearly eliminated a ~ 2-3 hPa P_{MIN} over-intensification bias in medium-to-long range forecasts. While short-range Control forecasts had a ~ 0.5 g kg^{-1} lower-tropospheric dry bias relative to aircraft reconnaissance mission dropsondes and ERA5, this dry bias was slightly stronger in ROMEX forecasts, consistent with the marginally weaker ROMEX-forecast storms. Notably, ROMEX assimilation reduced a large fraction of Control's persistent 10-20 hPa P_{MIN} over-intensification bias in short-to-medium range forecasts of Hurricane Fiona (2022) initialized on 21 and 22 September, when

Deleted: ; Ryglicki et al. 2018
Deleted: explains
Deleted: Although
Deleted: is currently near peak
Deleted: ,
Deleted: begins
Deleted: ning soon thereafter
Deleted: ,
Deleted: likely due to downshear displacement of its midlevel warm core as the vortex starts to tilt (Frank and Ritchie 2001) and the entrainment of midlevel dry air (Simpson and Riehl 1958; Cram et al. 2007) lurking in the upshear (southwestern) quadrant (Figs. 14c, 14d). The results shown in Fig. 14 suggest that beginning around 12 UTC 23 September, the environmental VWS becomes an increasingly important driver of Fiona's intensity and structure, outweighing the impact of subtle changes in the analysis of the water vapor field. Like TC steering flows, environmental VWS is mostly driven by larger-scale wind fields surrounding the storm
Deleted:
Deleted: data assimilation in
Deleted:
Deleted: .
Deleted: Therefore, it is not surprising to see
Deleted: er
Deleted: Fiona
Deleted: when VWS becomes stronger
Formatted: Line spacing: 1.5 lines
Deleted: for
Deleted: in
Deleted: addition
Deleted: to
Deleted: .
Deleted:
Deleted: While Spire data are known to have
Deleted: a
Deleted: lower signal-to-noise ratio
Deleted: than
Deleted:
Deleted: COSMIC-2
Deleted: ,
Deleted: derived
Deleted: ,

the TC was approaching its peak intensity. ROMEX analyses were about 0.25-1 g kg^{-1} drier in the lower-to-middle tropospheric TC core region than those of Control during this period, which likely helped to reduce the vigor of inner-core convection modestly, as was shown for the Fiona forecasts initialized at 12 UTC on 21 September.

The assimilated ROMEX observations reduced Control's specific humidity RMSD measured against ERA5 by ~ 1-5% in the mid-to-upper troposphere and showed a similar temperature RMSD improvement in the upper troposphere. However, lower-tropospheric temperature RMSD was slightly degraded up to t = 18 h. Additionally, ROMEX assimilation reduced the HAFS-A 750-950 hPa layer horizontal wind speed RMSD against dropsondes by ~ 1-2 m s^{-1}, demonstrating that the thermodynamic information provided by the additional RO observations can also improve HAFS-A forecast kinematic fields through cross-variate covariances in the DA system and/or dynamical adjustments during the cycled model advances. Assimilating the ROMEX data also yielded a modest *with al to* 5% relative skill improvement in medium-range forecast TC position errors, suggesting a slight improvement in the near-storm flow environment and vortex size. Track forecast impacts were likely limited because all HAFS-A experiments received the same larger-scale steering flow information supplied by the operational GFS to the outer domain's initial and lateral boundary conditions.

Two sensitivity experiments provided further insight. The Control_noC2 (Control without COSMIC-2 data) showed that COSMIC-2 observations modestly improved track, short-range P_{MIN} intensity, and lower- to mid-tropospheric water vapor forecasts, but had small and mixed impacts on temperature forecasts. The ROMEX_noLowlevRO experiment, which excluded all RO data below the 5-km impact height, assessed the value of assimilating lower-tropospheric RO data. Despite HAFS-A rejecting a large fraction of sub-5 km RO observations, those assimilated in ROMEX contributed to ≳ 50% its P_{MIN} relative skill improvement over Control in short-range forecasts. Although removal of the sub-5 km RO observations alleviated the modest ROMEX temperature and water vapor RMSD degradations against ERA5 found in the lower troposphere, it also largely eliminated ROMEX's water vapor RMSD improvements over a deeper layer between 800 and 400 hPa.

In conclusion, this study demonstrates that a 3.5-fold increase in the number of assimilated GNSS RO profiles with the addition of commercial Spire and PlanetiQ observations has an overall beneficial impact on HAFS-A track, P_{MIN}, lower-tropospheric wind speed, and

Deleted: HAFS

Deleted: ≲

Deleted:

Deleted: marginally

Deleted: to-mid

Deleted: reject

Deleted: lower

Deleted: nearly quadrupling the volume of globally

Deleted: vailable

Deleted: data

Deleted: by adding

middle-to-upper-tropospheric temperature and water vapor forecasts for the four 2022 Atlantic TCs evaluated. However, the impacts of these assimilated commercial observations on HAFS-A P_{MIN} intensity varied substantially across the 84-forecast sample, with the most notable improvement (al$\gtrsim$ 50% reduction in over-intensification bias) found in short- to medium-range Fiona forecasts initialized on 21-22 September. Also, we should note that the statistical forecast error analysis described in Section 4 was heavily influenced by the long-lived Earl and Fiona cases, which spent most of their time as hurricanes outside the tropics. Considering the marked decrease in COSMIC-2 profile density with latitude in the extratropics (Ho et al. 2020b), the incremental benefits of assimilating additional RO data may be proportionally greater for TCs moving outside the tropics, given the more uniform latitudinal distribution of sun-synchronous polar orbiting Spire and PlanetiQ satellites (Anthes et al. 2024). Future studies evaluating larger TC samples could test this hypothesis. Additionally, by showing Control_noC2's short-range intensity and medium-range track forecast degradations relative to Control, this study supports previous work showing positive impacts of COSMIC-2 assimilation on regional model TC forecasts (Miller et al. 2023; Teng et al. 2023) and the need to sustain COSMIC-2-like coverage over the tropics in future RO satellite missions.

For future work, HAFS forecast impact studies with a larger number of hurricane cases, particularly those weighted more towards the tropics, would provide a more definitive assessment of the commercial value of RO data. A major limitation of this study's OSEs is that HAFS-A, by design, assimilates data only within its inner moving nest, measuring impacts only within the TC vortex and near-storm environment. The HAFS-A outer domain's initial and lateral boundary conditions are downscaled from the operational GFS. When interpreting our results, it is also worth noting that RO bending angles are nonlocal observations that depend primarily on atmospheric fields along the tangent point-centered ~200-km ray path, which is about one-sixth of the HAFS-A inner nest width. Although HAFS-A's one-dimensional bending angle forward operator uses only the vertical column of background data above the tangent point, the analysis impacts of observations assimilated near the nest's lateral boundaries could be limited by the boundaries, which truncate the horizontal spread of observation information by the regional background error covariance matrix. Miller et al. (2023), for example, showed that COSMIC-2 bending angles assimilated in HWRF could adjust lower-to-middle tropospheric analysis water vapor fields $\gtrsim$ 100 km away by over 0.3 g kg^{-1} (see their Fig. 10). Ideally, future

Deleted: to-

Deleted: especially

Deleted:

Deleted: data denial experiment

Deleted: only assimilates data in its inner moving nest,

Deleted: measuring only impacts

Deleted: within

Deleted: most

Deleted:

Deleted: ing

experiments would also vary the RO data assimilated into the GFS, allowing impacts from data further from the TCs to affect larger-scale steering flows or water vapor fields advected into the HAFS inner nest later in the forecast period. However, running GFS sensitivity experiments was not possible due to limited computational resources. Future improvements to the HAFS RO DA algorithm, such as its QC screening criteria, observation error specification, and the implementation of nonlocal bending-angle forward operators, could further enhance the benefits of assimilating commercial RO data alongside the backbone government missions.

Acknowledgements:

GPS dropsonde data were provided by the NOAA Atlantic Oceanographic and Meteorological Laboratory Hurricane Research Division in Miami, FL (USA). HAFS-A experiments were run on NOAA's Hera supercomputer (https://www.noaa.gov/organization/information-technology/hera). The authors also acknowledge the University of Maryland supercomputing resources (http://hpcc.umd.edu) used for performing additional analysis reported in this paper. This work was funded by a NOAA Grant NA19NES4320002 and NA24NESX432C0001 (Cooperative Institute for Satellite Earth System Studies - CISESS) at the University of Maryland/ESSIC. The scientific results and conclusions, as well as any views or opinions expressed herein, are those of the authors and do not necessarily reflect those of NOAA or the Department of Commerce.

Data Availability Statement:

Large input and output datasets from the OSEs described in this study are stored on the NOAA Research and Development High-Performance Computing System (RDHPCS) High Performance Storage System (HPSS; https://docs.rdhpcs.noaa.gov/data/storage.html). They include the HAFS-A gridded forecasts, operational GFS forecasts providing the outer domain's initial and boundary conditions, HAFS-GSI DA diagnostic files, and the ROMEX global dataset covering the four Atlantic TC forecasting periods. The latter consists of BUFR-file-formatted Level-2 commercial and government-mission GNSS RO bending-angle observations processed by EUMETSAT, except for COSMIC-2 data, which are processed by UCAR. Additionally, software used for generating the results presented in this study are stored on the University of Maryland Linux servers. These resources can be made available upon request, although

Deleted: ar

Deleted: advected

Deleted: data assimilation

Deleted: g

Deleted: s

Formatted: Font: Times New Roman, Not Bold, Not Italic

Deleted: NA19NES4320002

Deleted: The

Deleted: simulation

Deleted: datasets

Deleted:

Deleted:

Deleted:

Deleted: and

Deleted: NOAA Research and Development High-Performance Computing System and on restrictions apply to sharing and redistribution of the ROMEX RO dataset (https://irowg.org/ro-modeling-experiment-romex/). The HAFS-A model code repository is publicly available on GitHub at https://github.com/hafs-community/HAFS.

Author contributions:

WM, YC, and SH designed the experiments, and WM carried them out. YC, SH, and XS coordinated with EUMETSAT in obtaining the commercial ROMEX dataset, and they performed an initial GNSS RO observation quality evaluation. WM developed codes to process and plot the HAFS-A model output. WM also prepared the manuscript with contributions from all co-authors.

Deleted: for
Deleted: ing
Deleted: ting

Competing interests:

The contact author has declared that none of the authors has any competing interests.

References:

Anthes, R. A., J. Sjoberg, X. Feng, and S. Syndergaard, 2022: Comparison of COSMIC and COSMIC-2 Radio Occultation refractivity and bending angle uncertainties in August 2006 and 2021. *Atmosphere* 2022, 13, 790, https://doi.org/10.3390/atmos13050790.

——, C. Marquardt, B. Ruston, and H. Shao, 2024: Radio Occultation Modeling Experiment (ROMEX): Determining the Impact of Radio Occultation Observations on Numerical Weather Prediction. *Bull. Amer. Meteor. Soc.*, **105**, 1552–1568, https://doi.org/10.1175/BAMS-D-23-0326.1.

Blake, E. S., 2023: Tropical cyclone report: Hurricane Earl (AL062022). National Hurricane Center Tech. Rep., 18 pp. [Available online at https://www.nhc.noaa.gov/data/tcr/AL062022_Earl.pdf]

Bonavita, M., 2014: On some aspects of the impact of GPSRO observations in global numerical weather prediction. *Quart. J. Roy. Meteor. Soc.*, **140**, 2546–2562, https://doi.org/10.1002/qj.2320.

Bowler, N. E., 2020: Revised GNSS-RO observation uncertainties in the Met Office NWP System . *Quart. J. Roy. Meteor. Soc.*, **146**, 2274–2296, https://doi.org/10.1002/qj.3791.

Deleted: .
Formatted: Font: (Default) Times New Roman, 12 pt, Not Bold
Deleted: ¶
Deleted:
Deleted: .
Formatted: Font: Times New Roman, Font color: Blue
Formatted: Font: Times New Roman
Formatted: Font: (Default) PT Sans, Font color: Custom Color(RGB(137,68,3))
Field Code Changed

Braun, S. A., J. A. Sippel, and D. S. Nolan, 2012: The impact of dry midlevel air on hurricane intensity in idealized simulations with no mean flow. *J. Atmos. Sci.,* **69**, 236-257, https://doi.org/10.1175/JAS-D-10-05007.1.

Bucci, L., L. Alaka, A. Hagen, S. Delgado, and J. Beven, 2023: Tropical cyclone report: Hurricane Ian (AL092022). National Hurricane Center Tech. Rep., 72 pp. [Available online at https://www.nhc.noaa.gov/data/tcr/AL092022_Ian.pdf]

Cangialosi, J. P., 2023: Tropical cyclone report: Hurricane Julia (AL132022). National Hurricane Center Tech. Rep., 23 pp. [Available online at https://www.nhc.noaa.gov/data/tcr/AL132022_EP182022_Julia.pdf]

Chan, J. C. L., and W. M. Gray, 1982: Tropical cyclone movement and surrounding flow relationships. *Mon. Wea. Rev.*, **110**, 1354–1374, https://doi.org/10.1175/1520-0493(1982)110<1354:TCMASF>2.0.CO;2.

Chavas, D. R., J. A. Knaff, and P. Klotzbach, 2025: A simple model for predicting tropical cyclone minimum central pressure from intensity and size. *Wea. Forecasting*, **40,** 333-346, https://doi.org/10.1175/WAF-D-24-0031.1.

Chen, S.-Y., Y.-H. Kuo, and C.-Y. Huang, 2020: The impact of GPS RO data on predicting tropical cyclogenesis using a nonlocal observation operator: an initial assessment. *Mon. Wea. Rev.,* **148,** 2701-2717, https://doi.org/10.1175/MWR-D-19-0286.1.

Chen, X., Y. Wang, J. Fang, and M. Xue, 2018: A numerical study on rapid intensification of Typhoon Vicente (2012) in the South China Sea. Part II: Roles of inner-core processes. *J. Atmos. Sci.,* **75,** 235-255, https://doi.org/10.1175/JAS-D-17-0129.1.

Christophersen, H., J. Sippel, A. Aksoy, & N. L. Baker, 2022: Recent advancements for tropical cyclone data assimilation. *Ann NY Acad. Sci.*, *1517,* 25–43, https://doi.org/10.1111/nyas.14873.

Cram, T. A., J. Persing, M. T. Montgomery, and S. A. Braun, 2007: A Lagrangian trajectory view on transport and mixing processes between the eye, eyewall, and environment using a high-resolution simulation of Hurricane Bonnie (1998). *J. Atmos. Sci.,* **64**, 1835-1856, https://doi.org/10.1175/JAS3921.1.

Cucurull, L., J. C. Derber, and R. J. Purser, 2013: A bending angle forward operator for global positioning system radio occultation measurements. *J. Geophys. Res. Atmos.*,

Formatted: Line spacing: 1.5 lines
Deleted:
Field Code Changed
Formatted: Font: Times New Roman, Font color: Blue
Formatted: Font: Times New Roman
Deleted: .
Formatted: Font: (Default) PT Sans, Font color: Custom Color(RGB(137,68,3))
Deleted:
Deleted:
Deleted:
Deleted:
Deleted: .
Formatted: Font: Times New Roman
Formatted: Indent: Left: 0.5", First line: 0", Space After: 8 pt
Formatted: Font: Times New Roman
Formatted: Font: (Default) PT Sans, Font color: Custom Color(RGB(137,68,3))
Formatted: Font: Times New Roman
Formatted: Indent: Left: 0.5", Space After: 8 pt, Line spacing: Multiple 1.16 li
Deleted: .
Formatted: Font: Times New Roman
Formatted: Font: Font color: Custom Color(RGB(137,68,3))
Deleted: .
Formatted: Font: Times New Roman
Formatted: Font: Times New Roman
Formatted: Font: (Default) PT Sans, Font color: Custom Color(RGB(137,68,3))
Formatted: Left, Indent: Left: 0.5", First line: 0", Space After: 8 pt, Line spacing: Multiple 1.16 li
Deleted:
Deleted: .
Formatted: Font: Times New Roman
Formatted: Font: Times New Roman
Formatted: Font: (Default) PT Sans, Font color: Custom Color(RGB(137,68,3))
Formatted: Indent: First line: 0.5", Space After: 8 pt, Line spacing: Multiple 1.16 li
Deleted: .
Formatted ... [2]
Formatted: Font: Times New Roman
Formatted ... [3]

118, 14–28, https://doi.org/10.1029/2012JD017782.

——, 2015: Implementation of quality control for radio occultation observations in the presence of large gradients of atmospheric refractivity. *Atmos. Meas. Tech.,* **8,** 1275-1285, https://doi.org/10.5194/amt-8-1275-2015.

——, and R. J. Purser, 2023: An improved one-dimensional bending angle forward operator for the assimilation of radio occultation profiles in the lower troposphere. *Mon. Wea. Rev.*, **151,** 1093-1108, https://doi.org/10.1175/MWR-D-22-0073.1.

Desroziers, G., L. Berre, B. Chapnik, and P. Poli, 2005: Diagnosis of observation, background and analysis-error statistics in observation space, *Quart. J. Roy. Meteor. Soc.,* **131,** 3385–3396, https://doi.org/10.1256/qj.05.108.

DeMaria, M., 1996: The effect of vertical shear on tropical cyclone intensity change. *J. Atmos. Sci.,* **53,** 2076–2088, https://doi.org/10.1175/1520-0469(1996)053<2076:TEOVSO>2.0.CO;2.

——, M. Mainelli, L. K. Shay, J. A. Knaff, and J. Kaplan, 2005: Further improvements to the Statistical Hurricane Intensity Prediction Scheme (SHIPS). *Wea. Forecasting*, **20**, 531-543, https://doi.org/10.1175/WAF862.1.

Doyle, J. D., C. A. Reynolds, C. Amerault, and J. Moskaitis, 2012: Adjoint sensitivity and predictability of tropical cyclogenesis. *J. Atmos. Sci.,* **69**, 3535-3557, https://doi.org/10.1175/JAS-D-12-0110.1.

Dutta, S., Vandenberghe, F., Shao, H., Zhang, H., and J. Doe, 2019: Assessment of radio-occultation from multiple GNSS platforms: Operational and non-operational. *JCSDA Quarterly,* **62,** 33-37, https://doi.org/10.25923/w2dh-ep66.

Frank, W. M. and E. A. Ritchie, 2001: Effects of vertical wind shear on the intensity and structure of numerically simulated hurricanes. *Mon. Wea. Rev.,* **129,** 2249-2269, https://doi.org/10.1175/1520-0493(2001)129<2249:EOVWSO>2.0.CO;2.

Galarneau, T. J. Jr., and C. A. Davis, 2013: Diagnosing forecast errors in tropical cyclone motion. *Mon. Wea. Rev.,* **141,** 405-430, 10.1175/MWR-D-12-00071.1.

Harnisch, F., S. B. Healy, P. Bauer, and S. J. English, 2013: Scaling of GNSS radio occultation impact with observation number using an ensemble of data assimilations. *Mon. Wea. Rev.*, **141,** 4395–4413, https://doi.org/10.1175/MWR-D-13-00098.1.

Healy, S. B., Eyre, J. R., Hamrud, M., and Thépaut, J.-N., 2007: Assimilating GPS radio

Formatted: Font: (Default) Times New Roman, 12 pt
Deleted:
Formatted: Font: Times New Roman
Formatted: Font: (Default) PT Sans, Font color: Custom Color(RGB(137,68,3))
Formatted: Space After: 8 pt, Line spacing: Multiple 1.16 li
Deleted: .
Formatted: Hyperlink, Font: (Default) Times New Roman, 12 pt, Not Bold, Font color: Auto
Field Code Changed
Deleted:
Formatted: Font: Times New Roman
Formatted: Normal, Indent: Left: 0.5"
Formatted: Font color: Custom Color(RGB(137,68,3))
Deleted:
Formatted: Font: Times New Roman
Formatted: Font: PT Sans, Font color: Custom Color(RGB(137,68,3))
Deleted:
Formatted: Font: Times New Roman
Formatted: Font: (Default) Times New Roman, 12 pt
Formatted: Font: (Default) Times New Roman, 12 pt
Formatted: Font: PT Sans, Font color: Custom Color(RGB(137,68,3))
Deleted:
Formatted: Line spacing: 1.5 lines
Formatted: Font: Times New Roman, Font color: Blue
Formatted: Font: PT Sans, Font color: Custom Color(RGB(137,68,3))
Field Code Changed
Deleted: ¶
Deleted:
Formatted: Font: (Default) Times New Roman
Formatted: Font color: Black
Deleted:
Formatted: Font: Times New Roman
Formatted: Font: PT Sans, Font color: Custom Color(RGB(137,68,3))
Formatted: Border: Top: (No border), Bottom: (No border), Left: (No border), Right: (No border), Between : (No border)

occultation measurements with two-dimensional bending angle observation operators. *Quart. J. Roy. Meteor. Soc.*, **133,** 1213-1227, https://doi.org/10.1002/qj.63.

Ho, S.-P., R. A. Anthes, C.O. Ao, S. Healy, A. Horanyi, D. Hunt, A. J. Mannucci, N. Pedatella, W. J. Randel, A. Simmons, et al., 2020a: The COSMIC/FORMOSAT-3 Radio Occultation Mission after 12 Years: Accomplishments, Remaining Challenges, and Potential Impacts of COSMIC-2. *Bull. Amer. Meteor. Soc.* **101**, E1107–E1136, https://doi.org/10.1175%2Fbams-d-18-0290.1.

——, and Coauthors, 2020b: Initial Assessment of the COSMIC-2/FORMOSAT-7 Neutral Atmosphere Data Quality in NESDIS/STAR using in-situ and satellite data. *Remote Sens.*, **12,** 4099, https://doi.org/10.3390/rs12244099.

Jones, S. C., 1995: The evolution of vortices in vertical shear. I: Initially barotropic vortices. *Quart. J. Roy. Meteor. Soc.,* **121,** 821–851, https://doi.org/10.1002/qj.49712152406.

Lien, G.-Y., and Coauthors, 2021: Assimilation impact of early FORMOSAT-7/COSMIC-2 GNSS radio occultation data with Taiwan's CWB Global Forecast System. *Mon. Wea. Rev.,* **149,** 2171-2191, https://doi.org/10.1175/MWR-D-20-0267.1.

Liu, H., J. Anderson, and Y.-H. Kuo, 2012: Improved analyses and forecasts of Hurricane Ernesto's genesis using radio occultation data in an ensemble filter assimilation system. *Mon. Wea. Rev.,* **140**, 151-166, https://doi.org/10.1175/MWR-D-11-00024.1.

Liu, Z., C. S. Schwartz, C. Snyder, and S.-Y. Ha, 2012: Impact of assimilating AMSU-A radiances on forecasts of 2008 Atlantic tropical cyclones initialized with a limited-area ensemble Kalman filter. *Mon. Wea. Rev.,* **140,** 4017–4034, https://doi.org/10.1175/MWR-D-12-00083.1.

Liu, Q., X. Zhang, M. Tong, Z. Zhang, B. Liu, W. Wang, L. Zhu, B. Zhang, X. Xu, S. Trahan, L. Bernardet, A. Mehra, and V. Tallapragada, 2020: Vortex initialization in the NCEP operational hurricane models. *Atmosphere* 11, no. 9: 968, https://doi.org/10.3390/atmos11090968.

Lonitz, K., C. Marquardt, N. Bowler, and S. Healy, 2021: Final Technical Note of 'Impact assessment of commercial GNSS-RO data', ESA Contract Report.

Jarvinen, B. R., C. J. Neumann, and M. A. S. Davis, 1984: A tropical cyclone data tape for the North Atlantic basin, 1886-1983: Contents, limitations, and uses. NOAA Tech. Memo. NWS NHC 22, 21 pp., https://www.nhc.noaa.gov/pdf/NWS-NHC-1988-22.pdf.

Deleted: .

Formatted: Default Paragraph Font, Font: (Default) Times New Roman, 12 pt, Not Bold

Formatted: Font: Not Bold

Formatted: Hyperlink, Font: Times New Roman, 12 pt, Font color: Auto

Field Code Changed

Deleted: ¶
——, X. Zhou, X. Shao, Y. Chen, X. Jing, and W. Miller, 2023: Using the commercial GNSS RO¶
Spire data in the neutral Atmosphere for climate and weather prediction studies. *Remote* ¶
Sens., **15(19),** 4836.…

Formatted: Font: (Default) Times New Roman, 12 pt, Not Bold

Formatted: Font: Times New Roman, 12 pt

Formatted: Font: Times New Roman

Formatted: Font color: Custom Color(RGB(137,68,3))

Formatted: Indent: Left: 0.5", First line: 0"

Formatted: Indent: Left: 0.5", First line: 0", Border: Top: (No border), Bottom: (No border), Left: (No border), Right: (No border), Between : (No border)

Formatted: Font: Times New Roman

Formatted: Font: PT Sans, Font color: Custom Color(RGB(137,68,3))

Formatted: Font: (Default) Times New Roman, 12 pt, Not Bold, Underline, Font color: Blue

Field Code Changed

Kaplan, J., and M. DeMaria, 2003: Large-scale characteristics of rapidly intensifying tropical cyclones in the North Atlantic basin. *Wea. Forecasting*, **18,** 1093–1108, https://doi.org/10.1175/1520-0434(2003)018<1093:LCORIT>2.0.CO;2.

Kuo, Y. H., T. K. Wee, S. Sokolovskiy, C. Rocken, W. Schreiner, D. Hunt, and R. A. Anthes, 2004: Inversion and error estimation of GPS radio occultation data. *J. Meteorol. Soc. Jpn.*, **82**, 507-531, https://doi.org/10.2151/jmsj.2004.507.

Kursinski, E. R., G. A. Hajj, J. T. Schofield, R. P. Linfield, and K. R. Hardy, 1997: Observing Earth's atmosphere with radio occultation measurements using the Global Positioning System. *J. Geophys. Res.,* **102(D19),** 23429–23465, https://doi.org/10.1029/97JD01569.

Miller, W. J., Y. Chen, S.-P. Ho, and X. Shao, 2023: Evaluating the impacts of COSMIC-2 GNSS RO bending angle assimilation on Atlantic hurricane forecasts using the HWRF model. *Mon. Wea. Rev.,* **151,** 1821-1847, https://doi.org/10.1175/mwr-d-22-0198.1.

——, Y. Chen, S.-P. Ho, and X. Shao, 2025: Exploring the Value of Spire GNSS Radio Occultation bending angle assimilation for improving HWRF model forecasts of Atlantic hurricane intensity. *Weather and Forecasting,* **40,** 809-827, https://doi.org/10.1175/WAF-D-24-0092.1.

Molinari, J., J. Frank, and D. Vollaro, 2013: Convective bursts, downdraft cooling, and boundary layer recovery in a sheared tropical storm. *Mon. Wea. Rev.*, **141**, 1048–1060, https://doi.org/10.1175/MWR-D-12-00135.1.

Montgomery, M. T., and R. K. Smith, 2014: Paradigms for tropical cyclone intensification. *Aust. Meteor. Oceanogr. J.,* **64,** 37-66, https://doi.org/10.22499/2.6401.005.

Nolan, D. S., 2007: What is the trigger for tropical cyclogenesis? *Aust. Meteor. Mag.*, **56 ,** 241–266, https://doi.org/ 10.1071/es06025.

Pasch, R. J., B. J. Reinhart, and L. Alaka, 2023: Tropical cyclone report: Hurricane Fiona (AL072022). National Hurricane Center Tech. Rep., 60 pp. [Available online at https://www.nhc.noaa.gov/data/tcr/AL072022_Fiona.pdf]

Rotunno, R., and K. A. Emanuel, 1987: An Air–Sea Interaction Theory for Tropical Cyclones. Part II: Evolutionary Study Using a Nonhydrostatic Axisymmetric Numerical Model. *J. Atmos. Sci.,* **44,** 542-561, https://doi.org/10.1175/1520-0469(1987)044%3C0542:AAITFT%3E2.0.CO;2.

Ruston, B., and S. Healy, 2021: Forecast impact of FORMOSAT-7/COSMIC-2 GNSS radio

Deleted:
Formatted: Indent: Left: 0.5"
Formatted: Font: Times New Roman
Formatted: Font: PT Sans, Font color: Custom Color(RGB(137,68,3))
Formatted: Font: Times New Roman, 12 pt
Deleted: .
Formatted: Font: (Default) Times New Roman, 12 pt, Not Bold, Underline
Formatted: Font: (Default) Times New Roman, 12 pt
Formatted: Font color: Auto
Formatted: Indent: First line: 0"
Field Code Changed
Formatted: Font: Times New Roman, 12 pt
Deleted:
Formatted: Left
Formatted: Font: Times New Roman
Formatted: Font color: Custom Color(RGB(137,68,3))
Deleted:
Formatted: Indent: Left: 0.5"
Formatted: Font: Times New Roman
Formatted: Font: PT Sans, Font color: Custom Color(RGB(137,68,3))
Formatted: Font: Times New Roman, 12 pt
Formatted: Font: Not Italic, Font color: Auto
Formatted: Normal (Web)
Deleted:
Formatted: Font: Times New Roman, 12 pt
Formatted: Font: Times New Roman, 12 pt
Formatted: Font: Roboto, 9 pt, Font color: Custom Color(RGB(83,100,121))
Formatted: Line spacing: single
Deleted: .

occultation measurements. *Atmos Sci. Lett.,* **22**, e1019, https://doi.org/10.1002/asl.1019.

Schreiner, W. S., and Coauthors, 2020: COSMIC-2 radio occultation constellation: First results. *Geophys. Res. Lett.,* **47,** e2019GL086841, https://doi.org/10.1029/2019GL086841.

Simpson, R. H., and H. Riehl, 1958: Mid-tropospheric ventilation as a constraint on hurricane development and maintenance. *Proc. Tech. Conf. on Hurricanes*, Miami, FL, Amer. Meteor. Soc., D4.1–D4.10.

Trahan, S., and L. Sparling, 2012: An analysis of NCEP tropical cyclone vitals and potential effects on forecasting models. *Wea. Forecasting*, **27,** 744-756, https://doi.org/10.1175/WAF-D-11-00063.1.

Teng, H.-F., Y.-H. Kuo, and J. M. Done, 2021: Importance of midlevel moisture for tropical cyclone formation in easterly and monsoon environments over the western North Pacific. *Mon. Wea. Rev.,* **149,** 2449-2469, https://doi.org/10.1175/MWR-D-20-0313.1.

——, Y.-H. Kuo, and J. M. Done, 2023: Potential impacts of radio occultation data assimilation on forecast skill of tropical cyclone formation in the Western North Pacific. *Geophys. Res. Lett*., **50,** 1-10, https://doi.org/10.1029/2021GL096750.

Wang, X., D. Parrish, D. Kleist, and J. Whitaker, 2013: GSI 3DVar-based ensemble-variational hybrid data assimilation for NCEP Global Forecast System: Single-resolution experiments. *Mon. Wea. Rev.,* **141,** 4098-4117, https://doi.org/10.1175/MWR-D-12-00141.1.

Zhang, D.-L., Y. Liu, and M. K. Yau, 2001: A multiscale numerical study of Hurricane Andrew (1992). Part IV: Unbalanced flows. *Mon. Wea. Rev.,* **129,** 92-107, https://doi.org/10.1175/1520-0493(2001)129<0092:AMNSOH>2.0.CO;2.

Deleted: .

Formatted: Default Paragraph Font, Font: (Default) Times New Roman, 12 pt, Not Bold, Font color: Custom Color(RGB(118,118,118))

Formatted: Font: (Default) Times New Roman, 12 pt, Not Bold

Formatted: Font color: Auto

Formatted: Border: Top: (No border), Bottom: (No border), Left: (No border), Right: (No border), Between : (No border)

Deleted: Ryglicki, D. R., J. H. Cossuth, D. H. Hodyss, and J. D. Doyle, 2018: The unexpected rapid intensification of tropical cyclones in moderate vertical wind shear. Part I: Overview and observations. *Mon. Wea. Rev.,* **146,** 3773–3800.

Formatted: Font: Times New Roman

Formatted: Font color: Auto

Formatted: Indent: First line: 0", Border: Top: (No border), Bottom: (No border), Left: (No border), Right: (No border), Between : (No border)

Deleted: →

Formatted: Indent: Left: 0.5"

Formatted: Font: Times New Roman

Formatted: Font: PT Sans, Font color: Custom Color(RGB(137,68,3))

Formatted: Indent: Left: 0.5", First line: 0"

Formatted: Font: Times New Roman

Formatted: Font: PT Sans, Font color: Custom Color(RGB(137,68,3))

Deleted: .

Formatted: Font: (Default) Times New Roman, 12 pt, Not Bold, Underline

Formatted: Font: (Default) Times New Roman, 12 pt

Formatted: Font color: Auto

Field Code Changed

Formatted: Font: Times New Roman

Formatted: Indent: Left: 0.5", First line: 0"

Formatted: Font: PT Sans, Font color: Custom Color(RGB(137,68,3))

Deleted:

Formatted: Indent: Left: 0.5", Line spacing: 1.5 lines

Deleted: .

Formatted: Font: Times New Roman

Formatted: Font: Times New Roman

Page 23: [1] Deleted **William James Schouler Miller** **4/30/26 1:31:00 PM**

Page 37: [2] Formatted **William James Schouler Miller** **4/28/26 9:32:00 PM**

Left, Indent: Left: 0.5", Space After: 8 pt, Line spacing: Multiple 1.16 li

Page 37: [3] Formatted **William James Schouler Miller** **4/28/26 9:32:00 PM**

Font: (Default) PT Sans, Font color: Custom Color(RGB(137,68,3))